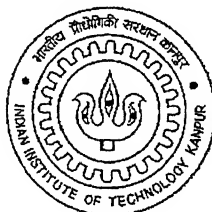


Enhanced Electrical Transport in KCl-KI System

*A Thesis submitted
in partial fulfillment of the requirement
for the Degree of*
MASTER OF TECHNOLOGY

By
Tathagata Bhattacharya



To the
**MATERIALS SCIENCE PROGRAMME
INDIAN INSTITUTE OF TECHNOLOGY, KANPUR
August 2002**

3 FEB 2003 / MSP

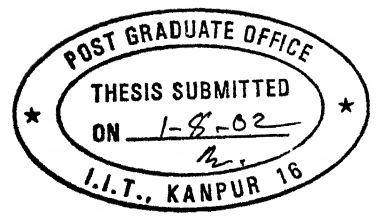
पुरुषोत्तम काशीनाथ केनकर पुस्तकालय

भारतीय प्रौद्योगिकी संस्थान कानपुर

अवधि क्र० A-141816



A141816



CERTIFICATE

It is to certify that the work presented in this thesis entitled *Enhanced Electrical Transport in KCl-KI System* by Tathagata Bhattacharya has been carried out under my supervision and this work has not been submitted elsewhere for a degree.

IIT Kanpur

August, 2002

(Prof. K. Shahi)

Thesis Supervisor

Materials Science Programme

IIT Kanpur

ABSTRACT

Most of the known superionic solids are silver based which are not cost effective. Therefore, it may be desirable to explore the possibility of enhancing the conductivity of so-called normal ionic solids so that they can be used as a substitute. Mixed ionic crystals have attracted considerable interest in recent times to this effect. With this motivation the KCl-KI mixed crystal system has been chosen for the present work. The binary system exhibits both solid solution as well as two-phase mixture region and the two alkali halides do not undergo any solid-solid phase transition. A maximum enhancement of conductivity by a factor of 430 and 169 (i.e., more than two orders of magnitude) with respect to pure KCl is observed at 400°C for KCl + 0.2 KI in the two-phase region and for KCl + 0.8 KI in the solid solution region respectively. The observed enhancement in conductivity cannot be explained on the basis of existing classical doping concept or by any law of mixtures. The significant enhancement of conductivity in the solid solution region is explained using the Lattice Loosening model on account of a large mismatch (21%) in the ionic radii of the host Cl^- and the dopant I^- ions. Percolation model explains the conductivity enhancement in the two-phase regime. Different techniques such as XRD, BET and FT-IR are used to characterize the samples besides complex impedance analysis, to extract dc electrical conductivity.

ACKNOWLEDGEMENT

At the very outset, I would like to convey my deepest gratitude to my guide Dr. K. Shahi for showing me the way through this journey of my thesis work. Without his invaluable guidance and constant encouragement the embodiment of my endeavor in the form of this thesis could have not been possible.

Only words will not suffice to express my sincere thanks to all my friends. I am extremely pleased to have friends like Gopinadhan, Aditi, Anisia, Santanu, Debadī, Abirda, Arnabda, Hochida, Chhanada, Pradiptoda, Seresta, Sidhu, Yadav, Pushpendra, Kamlesh, Praveendra, Sahooji, Ballu, Sanjay, Rahul, DJ, Pooja, Ruchi, Anurag, Dulal who were always there to help and support me and made my stay at IIT Kanpur a memorable one. Their warm association never allowed me to feel away from home whenever I was down and out.

I am really fortunate to have very nice persons like Anshuman, Jai, Mukesh and Abhishek around me as my labmates who spontaneously cooperated and encouraged me in situations of trouble.

I am grateful to Mr. Umashankar (X-ray Lab), Mr. T. B. Pandey (Solid State Ionics Lab), Mr. Sushanta Pal (Materials Testing Lab, BET), Mr. S. B. Pandey and Mr. K. Rajagopalan (Microanalytical Lab), Mr. Karthikeyan (Instrumentation Lab), Mr. Jai Kishan (Machine Shop), Mr. V. P. Sharma (Teaching Lab), Mr. Joshi (MSP Office), physics workshop staff Mr. Sampat Singh and central workshop superintendent and staffs for their incredible work which helped me to finish within time.

Last but not the least, I want to mark this memorable moment by fondly recalling the support of my family members and especially the fathomless love and ceaseless inspiration of my grandfather who is no more with us.

CONTENTS

Chapter1

Introduction	1
1.1 General Review	1
1.2 Types of Solid Ionic Conductors	2
1.3 Past Work	4
1.3.1 Stabilization of average or disordered structure	4
1.3.2 Dispersion of fine insulating particles	5
1.3.3 Doping	6
1.3.3.1 Aliovalent Doping	6
1.3.3.2 Homovalent Doping	6
1.4 Motivation and Scope of present work	10

Chapter2

Theoretical Aspects	11
2.1 Ionic conductivity of Pure Crystals	11
2.1.1 Concentration of Point Defects	12
2.1.1.1 Schottky Defects	12
2.1.1.2 Frenkel Defects	14
2.1.2 Mobility of Defects	15

2.1.3 Ionic Conductivity	16
2.2 Ionic Conductivity of (Aliovalently) doped Crystals	17
2.2.1 Concentration of Defects	17
2.2.2 Ionic Conductivity of Doped Crystals	19
2.2.3 Estimation of Transport Parameters	20
2.3 Theory of Ionic Conduction in (Homovalent) Mixed Crystals	22
2.3.1 The Lattice Loosening Model	22
2.3.1.1 Concentration of Defects in Mixed Crystals	22
2.3.1.2 Mobility of Defects in Mixed Crystals	26
2.3.1.3 Ionic Conductivity in Mixed Crystals	27
2.3.2 The Maximum Conductivity Composition	29
2.3.2.1 The Lattice Loosening Model	29
2.3.2.2 The $CB\Omega$ Model	29
2.3.2.3 The Percolation Model	31

Chapter3

Experimental Details and Characterization Techniques

32

3.1 Experimental Setup	32
3.1.1 Sample Holder	32
3.1.2 Furnace and Temperature Controller	34
3.1.3 Impedance Analyzer	34
3.1.4 Experimental Arrangement	35
3.2 Structural Analysis by X-ray Powder Diffraction (XRD)	37

3.3 BET Measurement	37
3.4 Fourier Transform Infrared Spectroscopy (FT-IR)	38
3.5 Complex Impedance Analysis	40
3.5.1 Pure Resistor	42
3.5.2 Pure Capacitive Circuit	42
3.5.3 Series Combination of R and C	43
3.5.4 Parallel Combination of R and C	44
3.6 Impedance Measurement Methodology	48
3.7 Materials Processing	51
3.8 Sample Preparation	51

Chapter4

Results & Discussion 54

4.1 X-ray Diffraction	55
4.2 BET Measurements	63
4.3 Fourier Transform Infrared Spectroscopy (FT-IR)	64
4.4 Complex Impedance Analysis	65
4.4.1 Conductivity vs. Temperature	65
4.4.2 Conductivity vs. Composition	74
4.4.3 Activation Energy & Knee Temperature vs. Composition	75
4.5 Discussion	82
4.6 Summary & Conclusion	93

References 97

List of Tables

<i>Table No.</i>	<i>Table Caption</i>	<i>Page No.</i>
1.1	Some selected superionic conductors with “average” or “molten” sub-lattice structure.	5
1.2	The electrical conductivity (σ_x) and the relative conductivity (σ_x/σ_o , σ_o being the conductivity of the pure component) at a fixed temperature T ($^{\circ}C$) of some selected mixed crystals.	9
2.1	Enthalpy of formation and migration of some ionic solids.	24
3.1	The Displays ‘A’ and ‘B’ of Impedance Analyzer.	35
3.2	The Physical Properties of the Starting Materials.	51
3.3	Sintering temperature, sintering time and thickness of different samples prepared (Pelletization pressure 4.0 tons/cm^2).	53
4.1	Lattice constant for different compositions of KCl-KI system.	61
4.2	Crystallite size for different compositions.	62
4.3	Various quantities involved in BET measurements.	63
4.4	Specific surface area of different samples.	64
4.5	Some impurity groups present in KI and their wave numbers.	65
4.6	Various transport parameters of $\text{KCl}_{1-x}\text{I}_x$ mixed crystals.	68
4.7	Magnitude of conductivity and enhancement factor	78

for three compositions at three different temperatures of KCl-KI system.

- | | | |
|-----|-----------------------------------------------------------------------------------------------------|----|
| 4.8 | Agreement of LL model with the experimental values obtained for KCl-KI mixed crystals. | 87 |
| 4.9 | Conductivity enhancement and mismatch factor for similar systems employing homovalent substitution. | 94 |

List of Figures

<i>Figure No.</i>	<i>Figure Caption</i>	<i>Page No.</i>
3.1	Sample holder for complex impedance analysis	33
3.2	Block diagram of the experimental set-up used in the ionic conductivity measurements	36
3.3	Impedance plot for a purely resistive circuit.	42
3.4	Impedance plot for a purely capacitive circuit	43
3.5	Impedance plot for a resistor and a capacitor in series	43
3.6 (a)	Impedance plot for a resistor and a capacitor in parallel	45
3.6 (b)	Effect of interface capacitance C_i on impedance of electrolyte	46
3.6 (c)	Effect of grain boundaries on the impedance of electrolyte	47
3.6 (d)	Depression of semicircle due to multiple polarizations	47
3.7	Impedance plots for KCl + 20m/o KI at four different temperatures	50
4.1 [a – e]	XRD plots for various composition of $\text{KCl}_{1-x}\text{I}_x$	56 - 58
4.2	Phase diagram of KCl-KI system re-plotted using the data obtained from literature	60
4.3	FT-IR spectroscopy of different compositions of $\text{KCl} + x\text{KI}$ ($0 < x < 1.0$)	66
4.4	Complex impedance plots for KCl + 0.80 m/o KI at four different temperatures	67
4.5 (a)	Variation of DC conductivity with inverse	69

	temperature for different compositions of KCl-KI system	
4.5 (b – j)	Fig. 4.5(b-j): Conductivity vs. inverse temperature for KCl + x m/o KI ($0 \leq x \leq 100$) system.	72
4.6	Variation of DC conductivity with inverse temperature for two samples of KCl + 20 m/o KI	73
4.7	Variation of DC conductivity with composition at three different temperatures for KCl + xKI ($0 < x < 1$)	76
4.8	Relative conductivity (σ_x/σ_0) as function of composition at three different temperatures	77
4.9	DC conductivity and migration enthalpy h_m plotted on the same graph against composition	79
4.10	Conductivity and activation energy E_a of intrinsic region plotted on the same graph against composition	80
4.11	Variation of knee temperature T_N and DC conductivity with composition plotted on the same graph	81
4.12–4.14	Comparison of Lattice Loosening model with the data obtained from experiment	83 - 85
4.15	Estimated melting temperature obtained from conductivity data. The solidus curve from available phase diagram has also been shown with the conductivity isotherm at 430°C	89
4.16	Isoconductivity plots for KCl - KI system. The solidus curve T_{mx} obtained from literature and the estimated melting curve from conductivity data can also be seen with one conductivity isotherm	90

Chapter1

Introduction

1.1 General Review

After Faraday propounded the laws of electrolytes, the need of ionic solids, where the charge transport occurs via movement of ions, for practical applications started brewing. Since 1967, a large number of such solids have been discovered and numerous applications were found such as solid state batteries, fuel cells etc. The conductivity, which plays a dominant role for their applications in solid state devices, paved a path to discover many ionic crystals.

Tubant *et al*^[1] found high ionic conductivity in AgI. They discovered that the conductivity of AgI in solid state is almost the same as that in the liquid phase. For practical applications, silver based ionic conductors cannot be used because of their cost unless it is absolutely essential.

The ionic conduction can be explained by the concept of lattice defect or interstitial ions. From the crystallographic point of view, a perfect ionic crystal would be an insulator. The movement of ions from one part of a perfect crystal to another part would be impossible if it were to occur only through direct exchanges between the anions and the cations. The energy which would have to be supplied to effect such a mechanism is so large ($\approx 15\text{ eV}$, for example in NaCl) that in one gram mole of the solid, such an event would occur only once in some $\approx 10^{30}$ years^[24]. In order to explain the ionic transport in solids, the presence of what is known as “point defects” was first invoked by Frenkel^[50]. He proposed that under the influence of thermal vibrations, the ions may occasionally receive enough thermal energy

to leave their normal place of residence (lattice site) and get pushed into a nearby void space (interstitial site), ordinarily not occupied by any ion. Under further thermal excitation, such an interstitial ion may jump from one interstitial position to another, until it finds a vacant normal site and drops into it. In presence of an electric field, the (positive) interstitial ions will jump more frequently in the field direction than in the opposite direction, giving rise to a net movement of charge (i.e., ionic conduction). Schottky^[51] developed a model in which there exists an equal number of anion and cation vacancies but no interstitial ions. Both Frenkel and Schottky type of point defects are now well accepted and constitute the basic foundation of the modern theories of ionic transport in solids which is the subject matter for chapter 2.

All silver halides like AgCl, AgBr etc. exhibit Frenkel defect while almost all alkali halides like KCl, KI, NaF etc. are known to show Schottky defect. In alkali halides, Mott and Littleton (1938) have calculated the heat of formation of Frenkel (H_F) and Schottky (H_S) defects. For example, in NaCl, they found $H_F = 2.9 \text{ eV}$ which is much larger than the value of $H_S (1.86 \text{ eV})$, and as a result, the concentration of Na^+ interstitials is negligible even at temperatures close to the melting point of NaCl. Thus NaCl, indeed all alkali halides, are said to exhibit Schottky type of defect.

1.2 Types of Solid Ionic Conductors

The solid ionic conductors can be classified on the basis of nature of charge carriers as:

- Cationic Conductors
- Anionic Conductors

Based on the structure, the solid ionic conductors can be clubbed into four classes:

- Crystalline Ionic Conductors
- Amorphous Solid Electrolytes
- Polymeric Solid Electrolytes
- Composite Solid Electrolytes

Based on the magnitude of conductivity of various solid ionic conductors, they can be grouped into three categories:

- Poor Ionic Conductors ($\sigma \leq 10^{-6} \Omega^{-1}cm^{-1}$) e.g., alkali halides.
- Moderate Ionic Conductors ($10^{-6} \leq \sigma \leq 10^{-3} \Omega^{-1}cm^{-1}$) e.g., AgBr, β -AgI, CaF₂, PbF₂, CaO.ZrO₂
- Superionic Conductors ($\sigma \geq 10^{-3} \Omega^{-1}cm^{-1}$) e.g., α -AgI, RbAg₄I₅, β -alumina etc.

The conductivity of ionic solids is a product of two exponential functions of temperature, concentration of defects and mobility of these defects (section 2.1). The mobility of defects in all normal salts lies in the range 10^{-4} to $10^{-6} cm^2V^{-1}s^{-1}$. Thus concentration of defects is largely responsible for determining the magnitude of conductivity of the solid ionic conductor at a given temperature. Thus the above classification can also be derived at on the basis of concentration of defects^[2].

On the basis of concentration of defects, the ionic conductors can be classified as under:

- Poor Ionic Conductors or Dilute Point Defect Type ($n \leq 10^{17}/cm^3$)

- Moderate Ionic Conductors or Concentrated Point Defect Type ($n \sim 10^{20}/\text{cm}^3$)
- Superionic Conductors ($n \sim 10^{22}/\text{cm}^3$)

1.3 Past Work

A great deal of work and research have already been undergone to develop solid state materials that exhibit high ionic conductivities due to their potential applications in solid state batteries, fuel cells, sensors etc. Several techniques have been adopted to enhance the conductivity of pure solids. The following discussion gives the idea about some of the major techniques employed for enhancement of conductivity in solid electrolytes:

1.3.1 Stabilization of “average” or disordered structure

High ionic conductivity observed in $\alpha\text{-AgI}^{[3,4,5]}$ has been attributed to its unique structure. It has bcc structure, in which anions (I^- ions) occupy the 8 corner $(0,0,0)$ as well as body center positions $(\frac{1}{2}, \frac{1}{2}, \frac{1}{2})$. There are now 42 interstitial sites available for two Ag^+ ions. The probability of occupancy of these sites is much less than unity. The situation is described as average structure.

$\alpha\text{-Li}_2\text{SO}_4$ is another superionic conductor which has the “average” structure, with β - α transition temperature at $\sim 575^\circ\text{C}$. Several efforts have been put into stabilizing its “average structure” at or near room temperature^[6,7]. Table 1.1 lists some superionic solids, which owe their high ionic conductivity to “average structure”.

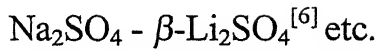
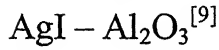
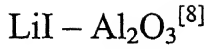
Table 1.1 Some selected superionic conductors with “average” or “molten” sub-lattice structure.

Compound	Mobile Ion	Ionic (β) – Superionic (α) transition temperature ($^{\circ}\text{C}$)	Conductivity σ ($\Omega^{-1} \text{cm}^{-1}$) at $T^{\circ}\text{C}$
α - Ag_2S	Ag^+	175	4.1 (200)
α - Ag_2Se	Ag^+	133	3.1 (200)
α - AgI	Ag^+	147	1.3 (150)
α - Ag_3SI	Ag^+	235	2 (240)
α - Na_2WO_4	Na^+	589	1.5×10^{-2} (800)
α - Li_2SO_4	Li^+	575	1.03 (600)

1.3.2 Dispersion of fine insulating particles

Liang^[8] was the first to report orders-of-magnitude enhancement in the conductivity of LiI due to dispersion of fine insulating Al_2O_3 particles. Subsequently, the effect was found to be quite general, not just limited to dispersion of insulating particles such as Al_2O_3 , SiO_2 , fly-ash etc., but even dispersion of AgBr solid solution in β - AgI ^[9], Na_2SO_4 ^[6] solid solution in β - Li_2SO_4 etc., were found to enhance the conductivity significantly. Such highly conducting materials have shown good promise for high energy density batteries and are now popularly called “composite solid electrolytes”.

Some examples of composite solid electrolytes are given overleaf:



1.3.3 Doping

1.3.3.1 Aliovalent Doping

Aliovalent doping is doping with ions whose valency is different from that of the host ion. Koch and Wagner^[10], Kelting and Witt^[11], Teltow^[12] have reported enhancement in conductivity of solid ionic conductors due to aliovalent dopants. An aliovalent dopant increases the concentration of certain kind of defects, as demanded by the charge neutrality condition.

1.3.3.2 Homovalent Doping

Substitution of ions having the same valency as that of the corresponding host ion also has a tremendous effect on conductivity. The enhancement in conductivity depends on the concentration and the relative size of the dopants. There always exists a size difference between the dopant and the host. The size mismatch factor δ is defined as

$$\delta = \left| \frac{r_i}{r_h} - 1 \right|$$

where r_i and r_h are ionic radii of the impurity (dopant) and the host ions respectively. Larger the mismatch factor δ , higher is the enhancement in conductivity.

The conductivity of $\text{LiI}_{0.75}\text{Br}_{0.25}$ was found to be $\sim 5 \times 10^{-7} \Omega^{-1} \text{cm}^{-1}$ at 293°K , which is higher than the pure components at the same temperature (Table 1.2). Apart from the conductivity enhancement the homovalent dopants are found to decrease the transition temperature as observed by Shahi and Wagner^[14] in $\beta\text{-AgI} - \text{AgBr}$ mixed crystals. The same effect was observed by Ihara *et al*^[16] (Table 1.2) in $\text{AgI}_{1-x}\text{Cl}_x$ ($0 \leq x \leq 1.0$) in the temperature range $60\text{-}200^\circ\text{C}$. The effect of Cl^- ions is more pronounced than that of Br^- ions because of large mismatch in case of the former. For various other mixed crystals studied so far, the conductivity enhancement is shown in Table 1.2. An inspection of this data will reveal the fact that for a particular composition of dopant, the conductivity attains a maximum value. This is consistent with the phase diagram which exhibits a minimum for the composition, implying the maximum possibility of increment in defect concentration at any temperature.

A semi quantitative model, viz., “Lattice Loosening Model”^[15] explains the transport properties in mixed crystals. Since the host and the dopant ions have the same valency, classical doping concept cannot be used to explain the observed enhancement in conductivity. Shahi and Wagner^[15] have argued that both the concentration and mobility of the defects affect the enhancement in conductivity. According to the Lattice Loosening Model, the substitution of the homovalent ions which are either larger or smaller than the host ions, usually leads to a decrease in the melting temperature as supported by phase diagrams and hence in formation and migration energies of defects.

The role of wrong size (mismatch factor δ) can be further gauged from the following observations. The conductivity enhancement in KCl–KBr with a low mismatch factor of $\sim 8\%$ is only by a factor of 2, whereas in CsCl – 70 *m/o* TlCl with a higher mismatch factor of $\sim 13\%$ the enhancement in conductivity is $\sim 7 \times 10^3$ at 387°C . Hence it is desirable to study the effect of wrong size substitutions on the ionic transport in mixed crystal systems. The substitution of too large or too small ions might cause the host ions around the dopant to readjust in order to allow the dissolution. Thus the elastic displacement so produced is likely to weaken the bonding between the atoms or cause lattice loosening.

Varotsos^[20,21,22,23] has proposed a purely thermodynamical theory, called CB Ω Model, which predicts, among other things, the composition of the mixed crystal which exhibits maximum conductivity and diffusion coefficient. This model which works well for some systems, fails to explain the observed behavior for several other mixed crystals. Besides a major disadvantage of this model is that it does not predict the magnitude of σ enhancement. This model along with the Lattice Loosening Model has been discussed in chapter 2 in more details with quantitative approach.

Table 1.2 The electrical conductivity (σ_x) and the relative conductivity (σ_x/σ_o , σ_o being the conductivity of the pure component) at a fixed temperature T ($^{\circ}C$) of some selected mixed crystals.

Mixed Crystals	Conductivity σ_x ($\Omega^{-1}cm^{-1}$)	σ_x/σ_o	Temperature ($^{\circ}C$)
KCl + 70 m/o RbCl ^[10]	5.5×10^{-5}	5	660
KBr + 50 m/o KI ^[9]	2.9×10^{-4}	63	500
LiBr + 40 m/o LiI ^[11]	1.8×10^{-6}	34	385
NaCl + 47 m/o NaBr ^[12]	8.0×10^{-5}	10	393
CsCl + 70 m/o TlCl ^[13]	5.6×10^{-2}	7×10^3	387
AgI + 40 m/o AgBr ^[14]	4.3×10^{-6}	16	25
AgBr + 30 m/o AgI ^[15]	6.5×10^{-6}	77	25
AgI + 10 m/o AgCl ^[16]	7.9×10^{-5}	125	25
LiBr + 75 m/o LiI ^[17]	5.0×10^{-7}	80	25
KCl + 50 m/o NaCl ^[18]	8.0×10^{-6}	80	500
KBr + 70 m/o NaI ^[19]	2.5×10^{-4}	500	500

1.4 Motivation and Scope of Present Investigation

Most of the known superionic solids are silver based which are not cost effective. Therefore, it may be desirable to explore the possibility of enhancing the conductivity of so called normal ionic solids so that they may be used as a substitute. With this motivation, one such alkali halide system namely KCl–KI is chosen for the present work. Apart from this the binary system exhibits both solid solution as well as two-phase mixture region and the two alkali halides do not undergo any solid-solid phase transition. K^+ ions are lighter and highly electro positive and thus can be used for high energy density batteries. KCl-KI system has been investigated because of large mismatch in the ionic radii of chloride and iodide ions (1.81\AA and 2.20\AA respectively, mismatch factor $\delta = 21\%$), thus expecting a large conductivity enhancement in the solid solution region, as suggested by the Lattice Loosening Model. Thus, in a nutshell, the aim of the present work may be stated as below:

- To enlarge the available data on mixed crystals.
- To study the effect of homovalent dopant namely KI on the ionic transport properties of KCl.
- To show the effect of wrong size of the dopant and the host (size mismatch) on the conductivity.
- To test the validity of the Lattice Loosening Model and the $CB\Omega$ Model developed for mixed crystals.

Chapter 2

Theoretical Aspects

2.1 Ionic Conductivity of Pure Crystals

The motion of charged defects in an electric field gives rise to an ionic conductivity, which usually dominates the electrical behavior of an ionic crystal because electronic conductivity is absent. The general form of Ohm's law says that the current density is proportional to the electric field

$$J = qV_{drift}n = q\mu nE = \sigma E \quad (2.1)$$

Here J is the current density, q is the charge on the defect, n is the concentration of defects, μ is the mobility of defects, V_{drift} is the drift velocity acquired by the charge carrier in the presence of an external electric field, E and σ is the conductivity.

Therefore the expression for conductivity is given by,

$$\sigma = nq\mu \quad (2.2)$$

For MX type of ionic solids, the total conductivity should include contribution from both positively and negatively charged defects. So the most general expression for conductivity of an ionic solid is

$$\sigma = \sigma_+ + \sigma_- = n_+q\mu_+ + n_-q\mu_- \quad (2.3)$$

Where the symbols have their usual meanings.

2.1.1 Concentration of point defects

As pointed out earlier, to explain the presence of ionic conduction, the concept of point defects was invoked. At absolute temperature (i.e. $T = 0K$), every crystal is free of point defects. At $T > 0K$, there is always a certain (finite) concentration of defects owing to thermal agitations. A large number of solids exhibit Schottky type of defect (cation and anion vacancies in equal number; for example, in monovalent salts like alkali halides). Frenkel type of defect is usually exhibited by silver halides, many oxides, rare earth fluorides, etc.

2.1.1.1 Schottky Defects

The production of Schottky defects, for example in alkali halides (MX), can be represented by the following reaction[#]:



The condition of electroneutrality requires Schottky disorder to occur with the formation of equal number of cation (n_c) and anion (n_a) vacancies, i.e., $n_c = n_a = n_s$ (say). This increases the configurational entropy (S_{cf}) given by:

$$S_{cf} = k \ln \left[\frac{(N + n_s)!}{N! n_s!} \right]^2 \quad (2.5)$$

[#]Kroger (1970) notation has been used for representing the defects.

where k is the Boltzmann constant, and the term inside the bracket gives the number of ways in which the n_s Schottky defects can be arranged over N lattice sites. The free energy change ΔG associated with the formation of Schottky defects is then given by^[24]

$$\Delta G = n_s g_s - kT \ln \left[\frac{(N + n_s)!}{(N! n_s!)} \right]^2 \quad (2.6)$$

The equilibrium concentration of defects is then obtained by the usual procedure of minimizing the free energy change (i.e., $\frac{\partial \Delta G}{\partial n} = 0$). In the approximation $n_s \ll n$, we get

$$\left[\frac{n_c}{N} \right] \left[\frac{n_a}{N} \right] = e^{\left(\frac{-g_s}{kT} \right)} \quad (2.7)$$

In terms of enthalpy (H_s) and entropy (S_s) of formation of Schottky defects ($g_s = H_s - TS_s$), the concentration of vacancies is given by

$$n_c = n_a \approx N e^{\left(\frac{S_s}{2k} \right)} e^{\left(\frac{-H_s}{2kT} \right)} \quad (2.8)$$

Eq. (2.7) is often considered to be an expression of law of mass action, i.e., the product of the concentration of anion and vacancies and of cation vacancies is a constant, equal to $\exp(-g_s/kT)$, at a given temperature. Eq. (2.7) is valid even if the two concentrations are unequal, as in case of a salt like PbI_2 and in aliovalently doped crystals.

2.1.1.2 Frenkel Defects

In MX type solids, the formation of (cationic) Frenkel defect is expressed as



Where V'_M stands for a negatively charged vacancy at the cation site and M^{\bullet}_i denotes the M ion (cation) with an effective positive charge, denoted by the superscript \bullet located at an interstitial site, denoted by the subscript i . The Gibb's free energy of the crystal containing n_F Frenkel defects is increased by an amount $n_F g_F$ (g_F is the free energy of formation of a Frenkel pair of defect), and simultaneously decreased by the configurational entropy arising from the disorder in the position of the interstitials and vacancies. For Frenkel defects, the equivalent of Eq. (2.6) is

$$\Delta G = n_F g_F - kT \ln \left[\frac{N!}{(N - n_F)! n_F!} \frac{N_i!}{(N_i - n_F)! n_F!} \right] \quad (2.10)$$

where N_i is the number of interstitial sites per unit volume. The usual minimization procedure gives (for $n_F \ll N, N_i$)

$$\left[\frac{n_i}{N_i} \right] \left[\frac{n_c}{N} \right] = \frac{n_F^2}{NN_i} = e^{\left(\frac{-g_F}{kT} \right)} \quad (2.11)$$

Once again, the product of the two concentrations is a constant at a fixed temperature. Substituting $g_F = H_F - TS_F$, where H_F and S_F are enthalpy and entropy of formation respectively, and $N_i = 2N$ for solids with rock salt structure, we get

$$n_i = n_c = n_F = 2^{1/2} N e^{\left(\frac{S_F}{2k} \right)} e^{\left(\frac{-H_F}{2kT} \right)} \quad (2.12)$$

2.1.2 Mobility of Defects

During the diffusion and ionic conduction process, the ions must move through the lattice from one site to another by jump process. The jump frequency w is expressed as^[25]

$$w = \nu e^{\left(\frac{-g_m}{kT}\right)} \quad (2.13)$$

where ν is the vibrational (attempt) frequency of the ions vibrating harmonically around their equilibrium positions and the migration energy g_m is the height of the barrier separating the two equivalent adjacent sites.

Consider a solid with NaCl-structure. An interstitial position will be available for the cation at a distance $a/2$ where a is the interionic distance. In presence of a DC electric field E the jump in the direction of the field takes place with an increased probability w^I (Lidiard^[24], Chandra^[2])

$$w^I = \nu e^{\left(\frac{(g_m - \frac{1}{2}eaE)}{kT}\right)} \quad (2.14)$$

and a jump against the field will take place with a reduced probability w^{II} given by

$$w^{II} = \nu e^{\left(\frac{(g_m + \frac{1}{2}eaE)}{kT}\right)} \quad (2.15)$$

The net number of ions moving per unit volume in the direction of field (assuming $eaE \ll kT$) is given by

$$n(w^I - w^{II}) = \frac{nweaE}{kT} \quad (2.16)$$

where n is the number of charge carriers per unit volume. The amount of charge passing per unit area per unit time, i.e., the current density is given by

$$j = \frac{na^2e^2wE}{kT} \quad (2.17)$$

Comparing Eq. (2.17) with $j = \sigma E = ne\mu E$, we get the following expression for mobility

$$\mu = \frac{a^2ew}{kT} \quad (2.18)$$

For vacancy conduction in NaCl type solids, the charge carrier has to jump a distance $2a$ in the field direction. Hence the mobility term will contain an additional numerical factor 4.

$$\mu = \frac{4a^2e}{kT} v_e e^{\frac{s}{k} - \frac{h}{kT}} \quad (2.19)$$

where h and s are enthalpy and entropy of migration respectively.

2.1.3 Ionic Conductivity

For ionic solids with rock salt structure in which the dominant type of defects are cation and anion vacancies (Schottky defect), the ionic (electrical) conductivity, i.e., Eq. (2.2) becomes

$$\sigma = e(n_c\mu_c + n_a\mu_a) \quad (2.20)$$

Substitution for the concentration n_c and n_a [Eq. (2.8)] and the mobilities μ_c and μ_a [Eq. (2.19)] leads to

$$\sigma = \frac{4Na^2e^2}{kT} \left[v_c e^{\left(\frac{s_s + s_{sc}}{2k} - \frac{h_s + h_{sc}}{kT}\right)} + \frac{4Na^2e^2}{kT} \left[v_a e^{\left(\frac{s_s + s_{sa}}{2k} - \frac{h_s + h_{sa}}{kT}\right)} \right] \right] \quad (2.21)$$

where e is the electronic charge and the subscripts s , c and a denote Schottky type, cation vacancy and anion vacancy respectively.

The above equation can be written in a simplified form as

$$\sigma T = A_c e^{\left(-\frac{E_{ac}}{kT}\right)} + A_a e^{\left(-\frac{E_{aa}}{kT}\right)} \quad (2.22)$$

Thus if more than one defect types are involved in the conduction, the σ vs. T dependence cannot be used to obtain any of the relevant transport parameters because of the complexity of Eq. (2.22). Fortunately, for most ionic solids, a particular type of defect dominates over the others (Friauf^[26]) and, in that case, Eq. (2.22) for a single conduction mechanism, can be written as

$$\sigma T = A e^{\left(-\frac{E_a}{kT}\right)} \quad (2.23)$$

For all alkali halides except for fluorides and cesium halides, the cation vacancies are the dominant charge carriers, and hence the parameters (A and E_a) in Eq. (2.23) can be assigned exclusively to cation vacancies.

2.2 Ionic Conductivity of (Aliovalently) doped Crystals

2.2.1 Concentration of Defects

The principle of doping the pure crystal with aliovalent impurities was first realized by Koch and Wagner^[27] and subsequently illustrated by Kelting and Witt^[28]; Teltow^[29] and others. Consider a solid whose intrinsic defect is either Schottky or Frenkel type. Let $x_c = n_c/N$ and $x_a = n_a/N$ be the molar

fractions of the two complementary defects (cation and anion vacancies). Eq (2.7) can be rewritten as

$$x_c x_a = x_{os}^2 = e^{-\left(\frac{g_s}{kT}\right)} \quad (2.24)$$

where x_{os} is the molar fraction of Schottky defects in the pure (undoped) solid. If C is the molar fraction of the aliovalent dopant (say C_{a+2} in a monovalent salt like NaCl), the condition for electroneutrality demands that

$$x_c = C + x_a \quad (2.24a)$$

Eq. (2.24) then becomes

$$x_c(x_c - C) = x_{os}^2 \quad (2.25)$$

which is a quadratic equation in x_c . The solution is

$$x_c = \frac{C}{2} \left[\left(1 + \frac{4x_{os}^2}{C^2} \right)^{\frac{1}{2}} + 1 \right] \quad (2.26)$$

Substituting this value of x_c in Eq. (2.24), we get

$$x_a = \frac{C}{2} \left[\left(1 + \frac{4x_{os}^2}{C^2} \right)^{\frac{1}{2}} - 1 \right] \quad (2.27)$$

When the concentration of the dopant C is large compared to that of thermally produced (intrinsic) defects (i.e., $C \gg x_{os}$) which is generally the case at lower temperatures, Eqs. (2.26) and (2.27) lead to

$$x_c \approx C \text{ and } x_a \approx \frac{x_{os}^2}{C} \ll 1 \quad (2.28)$$

Thus the concentration of one type of defects (cation vacancies, say) becomes nearly the same as that of the dopant (divalent cations, in the above

examples), and the concentration of the other (complementary) defect is made relatively negligible. The effect of doping was demonstrated most spectacularly in AgBr : Cd⁺² system by Teltow^[29].

At higher temperatures $x_{os} \gg C$ (intrinsic region), the Eqs. (2.26) and (2.27) yield

$$x_c = x_a = x_{os} = e^{\left(-\frac{g_s}{2kT}\right)} \quad (2.29)$$

which is the same as that for pure (undoped) crystal [Eq. (2.7)].

2.2.2 Ionic Conductivity of Doped Crystals

Since the mobility of the defects remains almost unaffected due to the presence of a small quantity of aliovalent impurity, the conductivity expression for a doped ionic solid exhibiting Schottky defects can be written as

$$\begin{aligned} \sigma = & \frac{4Na^2e^2}{kT} \nu_c \frac{C}{2} \left[\left(1 + \frac{4x_{os}^2}{C^2}\right)^{\frac{1}{2}} + 1 \right] e^{\left(\frac{s_{sc}}{k}\right)} e^{\left(-\frac{h_{sc}}{kT}\right)} + \\ & \frac{4Na^2e^2}{kT} \nu_a \frac{C}{2} \left[\left(1 + \frac{4x_{os}^2}{C^2}\right)^{\frac{1}{2}} - 1 \right] e^{\left(\frac{s_{sa}}{k}\right)} e^{\left(-\frac{h_{sa}}{kT}\right)} \end{aligned} \quad (2.30)$$

For $C \gg x_{os}$ (extrinsic region), the σ can be approximated by

$$\sigma T = \frac{4Na^2e^2}{k} \nu_c C e^{\left(\frac{s_{sc}}{k}\right)} e^{\left(-\frac{h_{sc}}{kT}\right)} \quad (2.31)$$

2.2.3 Estimation of Transport Parameters

Eq. (2.31) is in a much simpler form and thus permits the determination of transport parameters (h_{sc} and s_{sc}) associated with the cation vacancies, from the conductivity data on divalent cation doped samples. Likewise, ionic conductivity measurements on divalent anion doped solid yields information associated with anion vacancies. Thus σ vs. T data on pure, divalent cation doped and divalent anion doped solid leads to complete characterization of ionic transport processes.

The conductivity at high temperatures [intrinsic region, Eq. (2.23)] can be written as

$$\sigma_I = A_1 e^{\left(-\frac{E_1}{kT} \right)} \quad (2.32)$$

where

$$A_1 = \frac{4Na^2 e^2}{kT} \left[v_c e^{\left(\frac{s_s}{2k} + \frac{s_{sc}}{k} \right)} \right] \quad (2.33)$$

In low temperature (extrinsic) region, the conductivity [Eq. (2.31)] can be expressed as*

$$\sigma_2 = A_2 e^{\left(-\frac{E_2}{kT} \right)} \quad (2.34)$$

*The change in T is very small (by a factor of 2 to 3) compared to the change in sigma, which is of several orders of magnitude. Hence it is customary to write Eq. (2.23) in form of Eq. (2.32).

where

$$A_2 = \frac{4Na^2e^2}{kT} \left[\nu_c C e^{\left(\frac{s_{sc}}{k} \right)} \right] \quad (2.35)$$

Thus the slope of $\log \sigma_2$ vs. $1/T$ plot directly gives the activation energy E_2 , i.e., the enthalpy of migration of defects h and hence the mobility can be calculated from σ_2 ($= \sigma_{ext}$). Similarly, Eq. (2.32) gives the activation energy $E_1 = (H/2 + h)$ and hence H , the enthalpy of formation of the defects, can be obtained. By having a knowledge of ν_c , the pre-exponential factor A_1 and A_2 will give the formation and migration entropies of the defect. The knee temperature in the $\log \sigma$ vs. $1/T$ plot occurs at the temperature at which the concentration of intrinsic (thermally produced) defects x_{os} equals that of divalent dopants $x_{os} = C$.

In general the solubility of aliovalent impurities is always limited, particularly at lower temperatures. Thus, when a doped sample is cooled, the impurity phase may precipitate out at lower temperatures. In addition, a divalent cation impurity tends to form what is called impurity-vacancy pairs with the cation vacancies owing to their mutual attraction. Both the concentrations of the impurity-vacancy pairs and the solute (impurity phase) are temperature dependent. Thus the $\log \sigma$ vs. $1/T$ plot for a typical salt like alkali halide is a curve of constantly changing slope. The modern data analyses employ computer fit methods^[30,31] to obtain the best and the most consistent set of transport parameters.

2.3 Theory of Ionic Conduction in (Homovalent) Mixed Crystals

2.3.1 The Lattice Loosening Model

If the dopant has the same charge as the corresponding host ion, e.g., NaCl doped with KCl, the classical doping concept (see Sec. 2.2) cannot be used to explain any change (generally enhancement) in the conductivity. Even though a formal theory is yet to emerge, a semi-quantitative “Lattice Loosening Model”, based on certain empirical correlations observed in ionic solids, has been proposed by Shahi and Wagner^[9] and tested by Johannesen and McKelvy^[32,33] in KBr-KI and KCl-KBr systems.

According to the above model, the substitution of a wrong size ion generally introduces strain in the host lattice, and thereby weakens the bonding that eventually results in lowering of the melting point of the salt. That the phase diagrams of various binary systems generally exhibit a minimum in the melting point versus composition (liquidus/solidus) curves may be taken as evidence for it. Since the formation and the migration enthalpies of defects are correlated to the melting temperature of the solid^[34,35], the effect of wrong-size dopants ultimately is to decrease the formation and migration enthalpies of the point defects, and thus to increase both the concentration and the mobility of the point defects leading to enhanced ionic conductivity.

2.3.1.1 Concentration of Defects in Mixed Crystals

Whether the enhanced conductivity of the mixed crystals is due to increased concentration of charge carriers (defects) or due to enhanced mobility of the defects or due to a combined effect of both, has been a matter of

investigation. Wallace and Flinn^[36] reported as much as 1% of vacancies in KCl-KBr mixed crystals from X-ray density measurements. However, such a large defect concentration was found inconsistent with the conductivity results which led Haven^[52] to conclude that the above measurements must be in error. However, Holt *et al*^[37] have investigated the pure and divalent cation-doped KCl-RbCl mixed crystals, and reported an enhanced concentration of vacancies.

A semi-quantitative expression for the concentration of point defects in mixed crystals can be arrived at in view of the existing good empirical correlation between the enthalpy of formation H_s of Schottky defects and the melting point T_m of ionic solids. Table 2.1 lists the formation enthalpy H_s and melting point data for alkali, thallium and lead halides. As first pointed out by Barr and Lidiard^[34], H_s and T_m are linearly related

$$H_s = \alpha T_m \quad (2.36)$$

where α is the proportionality constant and has a value $\approx 2.14 \times 10^{-3} \text{ eV K}^{-1}$. Eq. (2.36) is an expression of the plain fact that stronger the bonding, higher is the melting point and hence more energy is required to displace the ions to form vacancies. Eq. (2.36) may be rewritten in the case of mixed crystals as

$$H_{sx} = \alpha T_{mx} \quad \text{or} \quad (H_{sx} - H_{so}) = \Delta H_{sx} = \alpha \Delta T_{mx} \quad (2.37)$$

where x refers to the concentration of the mixed crystals, and H_{sx} and H_{so} the formation enthalpies of mixed and pure crystals respectively. Eq. (2.37) expresses that the change in the formation enthalpy of the mixed crystal ($\Delta H_{sx} = H_{sx} - H_{so}$) with respect to that of pure crystal is proportional to the

Table 2.1 Enthalpy of formation and migration of some ionic solids^[26,34]

Salt	Melting Point (°C)	Enthalpy of Formation (eV)	Enthalpy of Migration (eV)	
			Cation Vacancies	Anion Vacancies
KCl	768	2.26-2.31	0.71	0.67-1.04
KI	680	0.6-0.22	0.6-1.21	0.5-1.5
KF	846	2.64-2.72	0.84-1.02	1.35-1.65
NaCl	800	2.18-2.38	0.66-0.76	0.9-1.1
NaF	992	2.42-3	0.52-0.95	1.46
NaI	661	1.46-2.27	0.47-0.78	-
NaBr	755	1.72	0.8	1.18
LiCl	606	2.2	0.41	-
LiF	842	2.34-2.68	0.65-0.73	1.1, 0.67

change in the melting point (ΔT_{mx}) of the mixed crystal T_{mx} with respect to that of pure crystal T_{mo} . The expression for the concentration of the Schottky defects [Eq. (2.8)] for mixed crystals can be rewritten as[⊕]

$$n_x = B_x e^{\left(-\frac{H_x}{2kT}\right)} \quad (2.38)$$

where B_x is a constant. Thus the ratio of the concentration of Schottky defects (n_x) in the mixed crystal to that in the pure crystal is given by

$$\frac{n_x}{n_o} = \frac{B_x}{B_o} e^{-\left(\frac{H_x - H_o}{2kT}\right)} \quad (2.39)$$

Substituting the value of $(H_x - H_o) = \Delta H_x = \alpha \Delta T_{mx}$ from Eq. (2.37) in Eq. (2.39) we get

$$\frac{n_x}{n_o} = \frac{B_x}{B_o} e^{-\left(\frac{\alpha \Delta T_{mx}}{2kT}\right)} \quad (2.40)$$

Thus the concentration of defects in the mixed crystals relative to that in pure crystal may be calculated from a knowledge of the change in the melting point ΔT_{mx} of the mixed crystal, provided the ratio of the pre-exponential factors

$$\frac{B_x}{B_o} = e^{-\left(\frac{s_x - s_o}{2k}\right)} \quad (2.41)$$

[⊕]Since the mixed crystal KCl-KI dealt in this thesis shows Schottky defects only, the subscript s is dropped henceforth.

can be calculated. We are not aware of any such calculation in mixed crystal. However, the entropies of formation of vacancies in the mixed crystal (s_x) and that in the pure crystal (s_o), in general, will not be very different, and hence their difference ($s_x - s_o$) is likely to be negligible. Thus B_x/B_o may be taken to be of the order of unity^[9,32], and Eq. (2.40) may then be written as

$$\frac{n_x}{n_o} \approx e^{-\left(\frac{\alpha \Delta T_{mx}}{2kT}\right)} \quad (2.42)$$

which expresses the relative concentration of vacancies as a function of the change in the melting point (ΔT_{mx}) of the mixed crystal. Since the melting point of the mixed crystal is generally less than that of the pure component, i.e., ΔT_{mx} is generally negative, Eq. (2.42) predicts an enhanced concentration of Schottky vacancies in the mixed crystal compared to that in the pure crystal.

2.3.1.2 Mobility of Defects in Mixed Crystals

In mixed crystals, mobility of ions also increases. A very good correlation between the enthalpy of migration of defects and the melting temperature was given by Barr and Lidiard^[38]. The h vs. T_m behavior is also found to be reasonably linear, and can be expressed by

$$h = \beta T_m - \gamma \quad (2.43)$$

where β ($= 0.84 \times 10^{-3} \text{ eVK}^{-1}$) and γ ($= 0.2 \text{ eV}$) are constants. For mixed crystals, Eq. (2.43) may be rewritten as

$$h_x = \beta T_{mx} - \gamma \text{ or } h_x - h_o = \Delta h_x = \beta \Delta T_{mx} \quad (2.44)$$

The ratio of the mobility of cation vacancies in the mixed crystals to that in the pure component may be written as [see Eq. (2.19)]

$$\frac{\mu_x}{\mu_o} = \frac{\nu_x}{\nu_o} e^{\left(\frac{s_x - s_o}{k}\right)} e^{-\left(\frac{h_x - h_o}{kT}\right)} \quad (2.45)$$

where ν_x and ν_o are the basic vibrational frequencies, and s_x and s_o , the migration entropies in the mixed and pure crystal respectively. To a first order approximation, we assume $\nu_x \approx \nu_o$ and $s_x \approx s_o$, so that

$$\frac{\mu_x}{\mu_o} \approx e^{-\left(\frac{h_x - h_o}{kT}\right)} \quad (2.46)$$

Substituting the value of $h_x - h_o = \Delta h_x = \beta \Delta T_{mx}$ from Eq. (2.44) in Eq. (2.46), one obtains

$$\frac{\mu_x}{\mu_o} \approx e^{-\left(\frac{\beta \Delta T_{mx}}{kT}\right)} \quad (2.47)$$

which predicts an enhanced mobility of vacancies as well in the mixed crystals as ΔT_{mx} is generally negative. The depression in the melting point at most is of the order of $100K$, i.e., $\Delta T_{mx} = -100K$, hence $-\beta \Delta T_{mx}/kT \approx 1.6$ at $600K$. Thus the maximum enhancement in the mobility of the defects in the mixed crystals is expected to be of the order of 5 or so.

2.3.1.3 Ionic Conductivity in Mixed Crystals

The ratio of the mobility of cation to that of anion vacancies in the mixed crystals remains almost the same as that in the component crystals over the entire composition range, as inferred from the diffusion coefficient

measurements in KBr-KCl^[39] mixed crystals. Thus if the cation vacancies are the more mobile species in the pure component, they are likely to remain so in the mixed crystals as well. Thus assuming that the cation vacancies are the dominant charge carriers, the ionic conductivity in mixed alkali halide crystals (σ_x) relative to that of pure crystal (σ_o) may be expressed as

$$\frac{\sigma_x}{\sigma_o} = \frac{n_x}{n_o} \frac{\mu_x}{\mu_o} \quad (2.48)$$

Substituting the value of (n_x/n_o) and (μ_x/μ_o) from Eqs. (2.42) and (2.47), we get

$$\frac{\sigma_x}{\sigma_o} \approx e^{\left[-\frac{\left(\frac{1}{2}\alpha + \beta \right) \Delta T_{mx}}{kT} \right]} \quad (2.49)$$

which on substituting the values of the constants α and β and the Boltzmann constant $k = 8.62 \times 10^{-5} \text{ eVK}^{-1}$, yields

$$\frac{\sigma_x}{\sigma_o} = e^{\left(-\frac{22.17 \Delta T_{mx}}{T} \right)} \quad (2.50)$$

The above equation which is based on the Lattice Loosening (LL) model and the empirical correlations between the enthalpies of formation and migration vs. T_m [Eqs. (2.36) and (2.43)] expresses the enhancement in σ_x of the mixed crystals relative to that of the pure crystal σ_o as a function of the change in the melting point due to the substitution of homovalent ions. An inspection of various binary alkali halide phase diagrams^[40] reveal that the lowering in the melting point ΔT_m ranges between 50 and 125°C. Eq. (2.50) would thus suggest that the enhancement in the conductivity of various mixed crystals

may be expected to be in the range ≈ 10 to ≈ 250 at $\approx 500K$ and ≈ 6 to ≈ 100 at $600K$. The data given in Table 1.2 are, by and large, in broad agreement with this prediction. Eq. (2.50) and the LL model will be further examined in Chapter 4 in view of the present investigation in KCl-KI system.

2.3.2 The Maximum Conductivity Composition

2.3.2.1 The Lattice Loosening Model

The LL model contained in Eq. (2.49) predicts the conductivity enhancement as a function of the depression in the melting point ΔT_{mx} . Thus if ΔT_{mx} is known as a function of composition, Eq. (2.49) can be used to predict the conductivity at any desired composition. It is obvious that within the LL model, the maximum conductivity composition would be same as that at which the melting point is minimum. In other words, the maximum in the σ_x vs. x plot would coincide with the minimum in the T_m vs. x plot of the phase diagram. The available experimental results, though very few, do support the above prediction.

2.3.2.2 The CB Ω Model

Varotsos^[21,22] has proposed a purely thermodynamic theory to predict the composition corresponding to the maximum enhancement in σ and diffusion constant D in the binary mixed crystal system. According to this model the ratio of the conductivity (or diffusion coefficient) of a mixed crystal to that of pure crystal is

$$\frac{\sigma}{\sigma_o} \text{ or } \frac{D}{D_o} = e^{-\left[\left(\frac{C_o B_o \Omega_o}{kT} \right) \left(\frac{CB\Omega}{C_o B_o \Omega_o} - 1 \right) \right]} \quad (2.51)$$

where

C, C_o = Constants.

B, B_o = Isothermal Bulk modulus of the mixed and pure crystal respectively.(i.e., $1/k$ and $1/k_o$, k and k_o being the compressibility of mixed and pure crystal respectively.)

Ω, Ω_o = Mean volume per atom of the mixed and pure crystal respectively.

The predicted composition x_m which will give maximum σ/σ_o is given by the following relation^[22]

$$x_m = \frac{\left(\frac{k_d}{k_o}\right) - 2}{\lambda \left(\frac{k_d}{k_o}\right)} \quad (2.52)$$

where

k_d = Compressibility of the defect volume.

k_o = Compressibility of the pure crystal.

$$\lambda = (V_I/V_o) - 1$$

The term “defect volume” and the symbols V_I and V_o are explained below.

Let v_o and v_I be the volume per molecule of the pure component-I and II respectively (assuming $v_I > v_o$) and let V_o and V_I denote their respective molar volume such that $V_o = Nv_o$ and $V_I = Nv_I$ where N is the Avogadro's number. The defect volume v^d is defined as the increase in volume V_o by replacing one molecule of component-I by one molecule of component-II, i.e., $v^d = v_I - v_o$.

The compressibility ratio, k_d/k_o can be derived from Born's model^[41].

The Eq. (2.52) has been found to predict x_m correctly for several systems, viz. NaCl-NaBr, KI-RbI, KI-NaI, KCl-RbCl and KBr-KI. The $CB\Omega$ model will be re-examined further for our present investigation in KCl-KI system in Chapter 4.

2.3.2.3 The Percolation Model

The Percolation model or the Random Resistor Network model (RRN) was proposed by Dieterich and coworkers^[47] and has successfully explained the enhancement in the conductivity of composite solid electrolytes. The RRN model assumes the existence of three types of regions (resistors) in the composite material, one is the insulating resistor representing the lack of conduction through insulating particles, next is the highly conducting resistors representing the enhanced interfacial conductivity and at last the normally conducting resistors representing the conduction in the pure ionic conductor. Thus one has the first two types of resistors in a matrix of normally conducting resistors. This is then mapped on to the problem of a random walk on a lattice with three types of bonds, and the diffusion constant is calculated by means of Monte Carlo simulations. The results of the simulations show that the enhanced conductivity starts at a critical concentration of the dispersed particles corresponding to the onset of percolation of highly conducting bonds. However, as the concentration increases, one encounters the second critical concentration where the conducting bonds start forming closed loops inside the system and the conductivity drops drastically leading to the conductor-insulator transition.

Chapter 3

Experimental Details and Characterization Techniques

3.1 Experimental Setup

3.1.1 Sample Holder

Fig.3.1 shows the schematic diagram of the sample holder. It consists of three identical lava discs (diameter ~ 2.5 cm and thickness ~ 1 cm), each having a central hole and four symmetrically located holes near the periphery. The lava discs, after machining were heated slowly to 1000°C and kept at that temperatures for two hours before cooling inside the furnace. This kind of heat treatment was necessary to harden the lava disc and also to remove any moisture content. Pair of stainless steel rods was passed through the two diametrically opposite holes to provide support to the sample holder. The spring which was so located that it remains outside the furnace, applied uniform pressure due to spring action to ensure a firm contact between the electrodes and the sample. A quartz tube was used to provide the body of the sample holder.

The flat surfaces of the cylindrical pellets were polished on different grades of fine polishing papers to remove the surface contamination and to obtain smooth and parallel surfaces. The surfaces were then coated with graphite paint, which will act as the electrodes. The pellet was carefully placed between the two silver electrodes. The spring mechanism ensures that there was a firm contact between the electrodes of the sample.

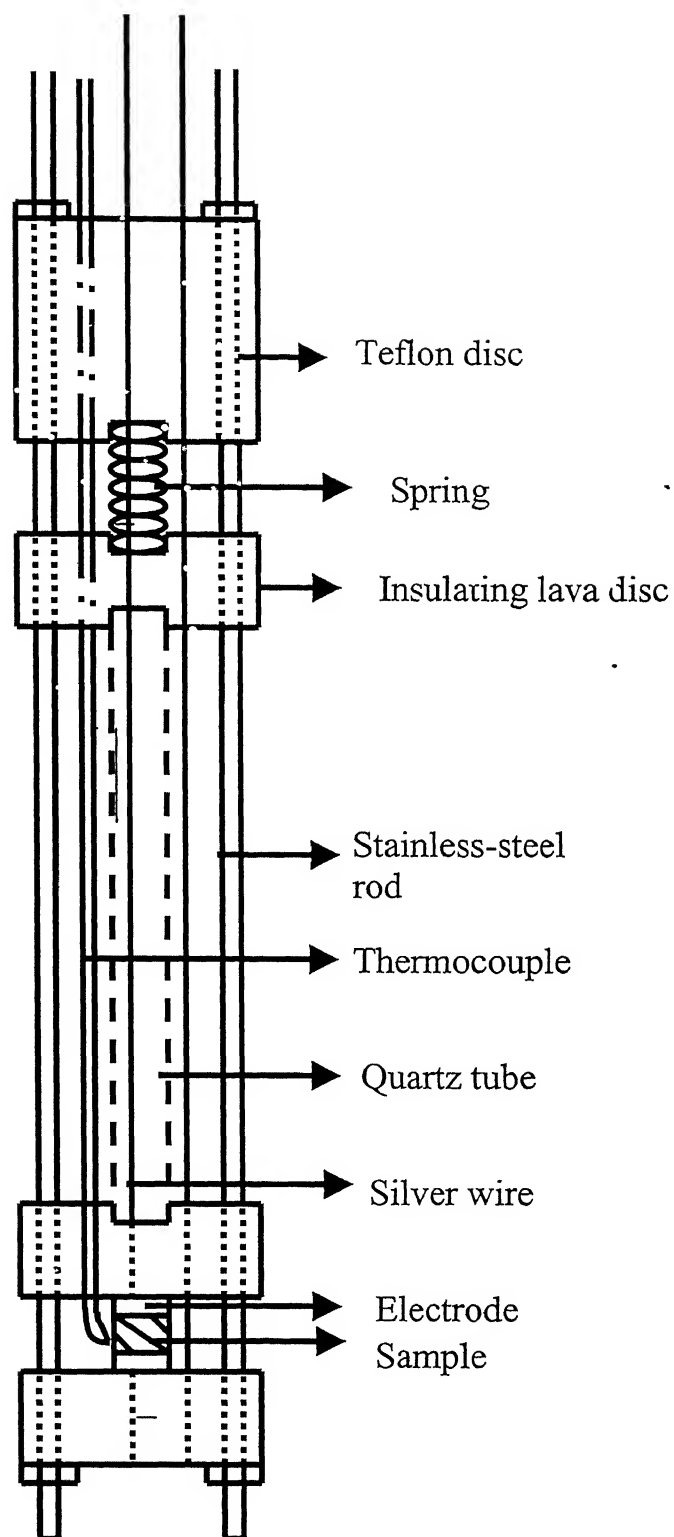


Fig. 3.1: Sample holder for complex impedance analysis

3.1.2 Furnace and Temperature Controller

An electrical resistance heating furnace comprising of a mullite tube (internal diameter ~ 4.9 cm), over which kanthal wire was wound uniformly, has been used. The resistance of the heating element was 28.2Ω . A high temperature cement was applied over the kanthal to fix it in place. The mullite tube with cemented kanthal wiring was enveloped with a cylindrical stainless steel container and the space between mullite tube and the steel container was filled with glass wool in order to minimize the heat loss.

A chromel-alumel thermocouple was employed to measure the temperature of the sample. A DMM is connected to output of this thermocouple and moreover a PID type temperature controller (Indotherm 401D) has been used to control the temperature of the furnace. A platinum-13% rhodium thermocouple has been used for providing feedback to the temperature controller, which compares set temperature & actual temperature and accordingly supplies the required power to the furnace. The accuracy of the DMM used is $1\mu V$.

3.1.3 Impedance Analyzer

HP 4192A fully automatic impedance analyzer along with a HP 1607A-test fixture is employed for a wide range of complex impedance measurement.

Impedance analyzer is a small-signal AC measurement device with a wide range of frequencies to investigate the electrochemical properties of the solid electrolytes. The instrument has an auto balancing bridge with a test signal from 5 mV to 1 mV. One can sweep the frequency from 5 Hz to 13 MHz.

The two display modes 'A' or 'B' can be selected to measure the quantities of interest as in Table 3.1. Usually one uses a parallel mode of connection so that the resultant semicircle plot of $Z\cos\theta$ and $Z\sin\theta$ can be utilized for calculating the resistance of the various components present in the circuit. Depending upon the presence of interfacial capacitance, and grain boundaries, the plot takes different shapes.

Table 3.1: The Displays 'A' and 'B' of Impedance Analyzer

Display A Function	Display B Function
Z : Absolute value of Impedance Y : Absolute value of Admittance	θ (deg/rad): Phase angle
R: Resistance	X: Reactance
G: Conductance	B: Susceptance
L: Inductance C: Capacitance	Q: Quality Factor D: Dissipation Factor R: Resistance G: Conductance

The equivalent circuit modes are auto, series and parallel, and one can select any of these depending upon ones interest.

3.1.4 Experimental Arrangement

The block diagram in Fig.3.2 shows the experimental set up for the conductivity experiments. The sample whose electrical or dielectric properties to be measured are made in the form a pellet by applying a force of 4 tons in the cylindrical form and after applying necessary graphite

coating, placed between the silver electrodes of diameter 11 mm in the sample holder. A special type of sample holder was constructed for this purpose. The silver electrodes are brazed to silver wires to provide connection to the impedance analyzer, and chromel–alumel thermocouple is attached with the sample holder to measure the temperature of the sample, which is connected to a Kiethly DMM (Digital Multimeter) which will measure the temperature as a function of voltage. From the calibrated tables one can calculate the temperature of the sample. A temperature controller (Indotherm 401D) is used to control the furnace temperature. The various components of this set up were discussed in detail above.

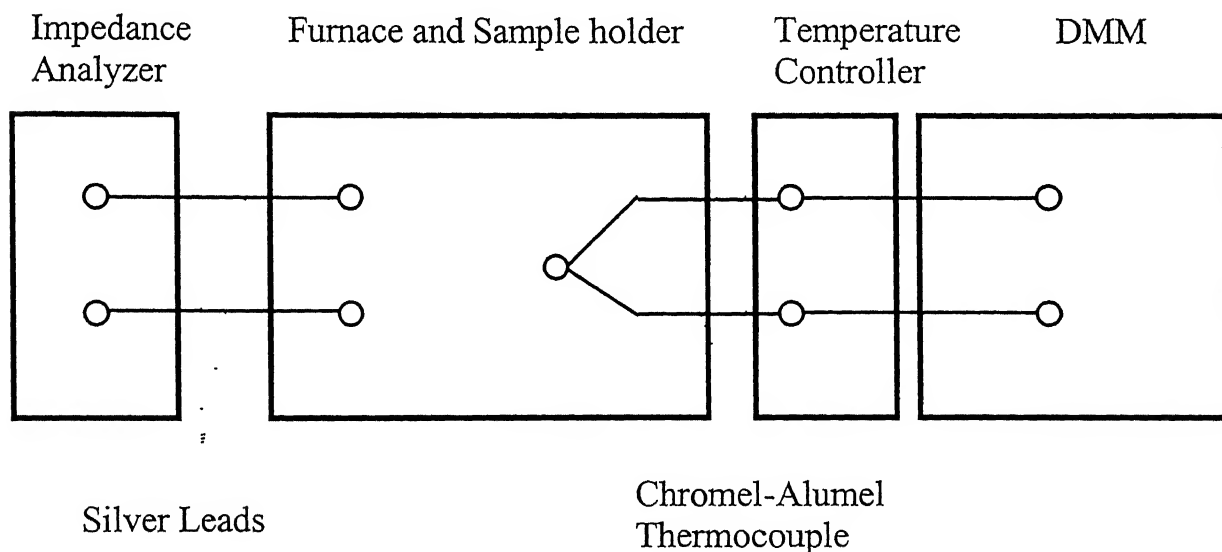


Fig. 3.2: Block diagram of the experimental set-up used in the ionic conductivity measurements

3.2 Structural Analysis by X-ray Powder Diffraction (XRD)

Phases present in a material are important as it is directly related to its electrical properties. In order to identify the various phases present in the samples containing the various mole fractions of KCl and KI, X-ray diffraction patterns have been taken and analyzed.

The X-ray diffraction patterns of various compositions were recorded using a computerized Richeifert (ISO-DEBYEFLEX 2002D) powder diffractometer using a filtered $\text{CuK}_\alpha (\lambda = 1.542 \text{ \AA})$ radiation. The generator was operated at 30 kV and 20 mA . The scanning speed was $3^\circ/\text{min}$ in 2θ . All XRD patterns were recorded at room temperature.

3.3 BET Measurement

The BET (Brunauer, Emmet and Teller) calculation was first introduced in 1938. It is the most commonly used characterization of specific surface area. The BET surface area (which includes all internal surfaces) is calculated from a multilayer adsorption theory. The method may be defined simply as the physical characterization of material structures using a process where gas molecules of known size are condensed and the resultant sample pressure are recorded and used for subsequent calculation. This data, when measured at constant temperature, allows an isotherm to be constructed. Isotherm data is then subjected to a variety of calculation models to obtain surface area.

The BET equation should produce a straight line plot, the linear form of which is most often represented as:

$$\frac{P_s}{V_A(P_O - P_s)} = \frac{1}{V_M C} + \left[\frac{C-1}{V_M C} \right] \times \frac{P_s}{P_O} \quad (3.1)$$

where: V_M = Volume of monolayer
 V_A = Volume adsorbed
 P_S = Sample pressure
 P_O = Saturation pressure
 C = Constant related to the enthalpy of adsorption

A specified relative pressure range (usually 0.05 to 0.2) is chosen and the isotherm data is used to calculate the BET function, which is plotted against relative pressure (P_S/P_O). To give a straight line having a slope $[(C-1)/V_M C]$ and intercept $(1/V_M C)$.

The BET surface area in (m^2/g) is then determined from the following expression:

$$S_{BET} = \frac{V_M \times N_A \times A_M}{M_V} \quad (3.2)$$

where S_{BET} is the BET surface area, N_A is Avogadro number, A_M is the cross sectional area occupied by each adsorbate molecule, and M_V is the gram molecular volume (22414 mL). For nitrogen BET determination, the cross-sectional area of the adsorbate molecule is assumed to be 0.162 nm^2 .

3.4 Fourier Transform Infrared Spectroscopy (FT-IR)

The broadband spectra like Raman and IR are presently becoming more popular as the useful tools to study the structural aspects of the material under study, which are sensitive to compositional variations. Infrared spectroscopy, in particular involves the absorption of electromagnetic radiations by matter, the existence of which is known since a long time with the discovery of Sir William Herschel in 1800^[42]. Today Infrared spectroscopy ranges approximately from $0.78 \mu\text{m}$ ($1/\lambda = 12500 \text{ cm}^{-1}$) to $1000 \mu\text{m}$ ($1/\lambda = 10 \text{ cm}^{-1}$). However the most useful range is from $2 \mu\text{m}$ to $16 \mu\text{m}$.

The absorption bands, which occur in this region, are due to the fundamental molecular vibrations. Consequently they lend themselves to identification, qualitative analysis and band alignment.

It is well-accepted fact that the matter absorbs infrared radiations selectively with respect to the wavelength. The two necessary conditions, which must be met before the absorption of infrared radiations by the molecule can occur, are

- 1) There must be a change in dipole moment of a molecule, and this will occur only when the electrical charges on the atoms are unequally distributed. Under these conditions, a stationary alternating electric field is produced whose magnitude changes with the frequency; and it is this electric field which interacts with the field of electromagnetic radiations.
- 2) The molecular vibration frequency must be identical to that of incident electromagnetic radiation, failing which the radiations transmit through the molecule without any loss of energy.

As a result, when infrared radiations of successive frequencies are passed through the molecule and the fraction of transmitted energy is plotted against the frequency or wavelength, the result is a series of minima and maxima, which is referred to as an infrared absorption spectrum. The absorption or transmission of this electromagnetic energy is dependent on the number of atoms, their mass, their way of stacking in the material and the force constant of interatomic bonds. The vibrations between various atoms within the molecule could be described as stretching vibrations, bending vibrations, involving groups of atoms within the molecule and the vibrations of the molecule as a whole. These vibrations can occur at various frequencies and are characteristics of groups of atoms within the molecule. Thus, absorption

peaks at various wavelengths are correlated with the molecule, using which, the structural studies can be carried out. The depth of the absorption bands is directly related to the number of molecules in the beam of radiation, and this feature is often used for qualitative measurements.

The samples were prepared by grinding and then mixing thoroughly in an agate mortar. The Fourier Transform Infrared Spectroscopy (FT-IR) studies were carried out with a spectrometer model Vector-22 (Bruker) in the range $400\text{-}4000\text{cm}^{-1}$. Measurements were made on an amorphous material dispersed in KBr in the ratio 1:30.

3.5 Complex Impedance Analysis

Impedance Spectroscopy is a relatively new and powerful method of characterizing many of the electrical properties of materials and their interfaces with electronically conducting electrodes^[43]. It may be used to investigate the dynamics of bound or mobile charge in the bulk or interfacial regions of any kind of solid or liquid material: ionic, semiconducting, mixed electronic-ionic, and even insulators (dielectrics). The complex impedance data analysis can yield near-perfect estimates of bulk conductivity of the materials free from the electrode polarization effects, which are obtained from the steady state DC measurements. Impedance spectroscopy was first applied by Bauerle^[55] to study the basic polarization process in the cell of yttria stabilized zirconia. Since dc measurements involve polarization effects, ac measurements are used to extract the dc conductivity.

Impedance of a circuit is the ratio of voltage to the current as Ohm's law holds well in the time domain. If the voltage function is given by

$$V(t) = V_m \exp(j\omega t) \quad (3.3)$$

then the current function will be given by:

$$I(t) = I_m \exp[j(\omega t + \phi)] \quad (3.4)$$

The impedance of the circuit, $Z(\omega)$, has both magnitude $|Z|$, and phase angle ϕ and can be expressed in both polar and cartesian form;

$$\begin{aligned} Z(\omega) &= |Z| \exp(-j\phi) \\ &= |Z| \cos\phi - j|Z| \sin\phi \\ &= Z' - jZ'' \end{aligned} \quad (3.5)$$

where Z' and Z'' are real and imaginary parts of the complex impedance. Therefore the magnitude of complex impedance

$$|Z| = \sqrt{Z'^2 + Z''^2} \quad (3.6)$$

and the phase angle is given by

$$\phi = \tan^{-1}\left(\frac{Z''}{Z'}\right) \quad (3.7)$$

$$\text{Admittance, } Y = 1/Z(\omega) = G + jB \quad (3.8)$$

$$\text{Conductance, } G = \frac{Z'}{Z'^2 + Z''^2} = 1/R \quad (3.9)$$

$$\text{Susceptance, } B = \frac{Z''}{Z'^2 + Z''^2} = \omega C \quad (3.10)$$

The different types of contributions coming from the leads, electrolyte and the electrodes can be modeled as a combination of resistors and capacitors. The plot of Z_R vs. Z_I plots for various representative circuits are described below.

3.5.1 Pure Resistor

The real and imaginary parts of the complex impedance of a purely resistive circuit, with resistance R are given by

$$Z' = R, Z'' = 0 \quad (3.11)$$

The impedance plot i.e., the plot of Z'' vs. Z' will be a point at $Z' = R$

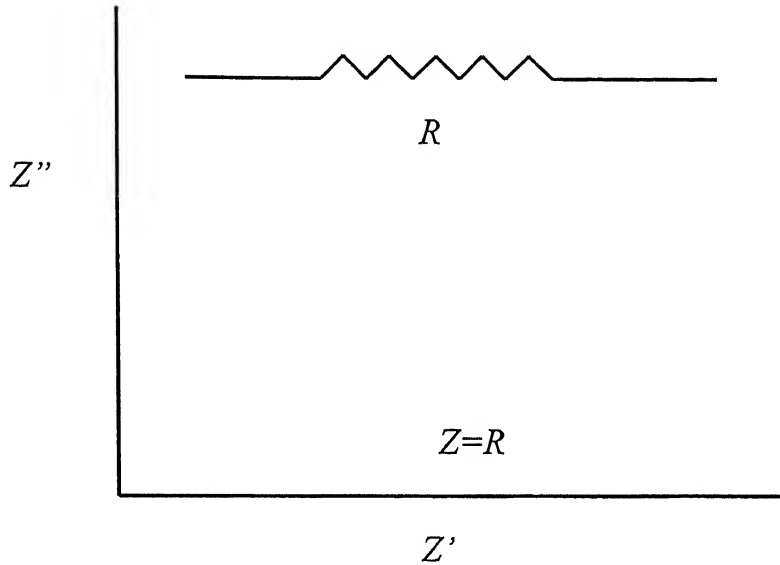


Fig. 3.3: Impedance plot for a purely resistive circuit.

3.5.2 Pure Capacitive Circuit

For a purely capacitive circuit, the real and imaginary parts of complex impedance are given by

$$Z' = 0; Z'' = -1/\omega C \quad (3.12)$$

The corresponding impedance plot will be a straight line parallel to negative Z'' axis at $Z'=0$. The impedance plot for a purely capacitive circuit is given in Fig. 3.4.

3.5.3 Series Combination of R and C

When the components behaving like a series combination of R and C , one gets

$$Z(\omega) = R - \frac{j}{\omega C} \quad (3.13)$$

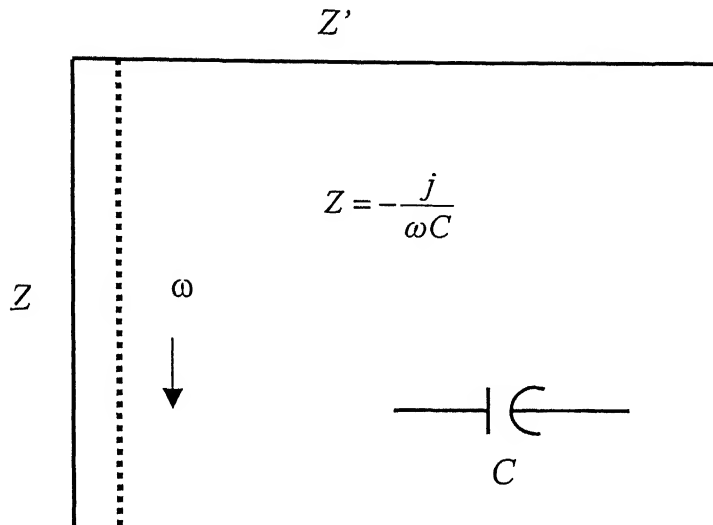


Fig. 3.4: Impedance plot for a purely capacitive circuit

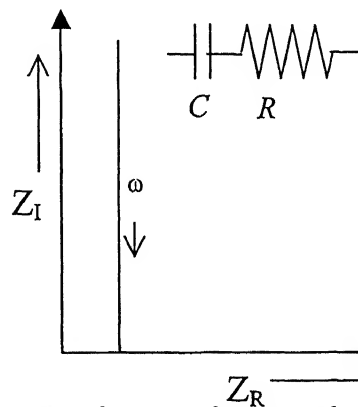


Fig. 3.5: Impedance plot for a resistor and a capacitor in series

$$Z = -\frac{j}{\omega C} \quad (3.14)$$

with

$$Z_R = R$$

$$Z_I = -\frac{1}{\omega C} \quad (3.15)$$

This essentially gives a straight line parallel to the negative imaginary axis at $Z' = R$, as shown in Fig. 3.5

3.5.4 Parallel Combination of R and C

If the system of various components can be modeled as a parallel combination of R and C , then we get

$$Z(\omega) = \frac{R \left(\frac{1}{j\omega C} \right)}{R + \left(\frac{1}{j\omega C} \right)} \quad (3.16)$$

$$= \frac{R}{1 + \omega^2 C^2 R^2} + j \left[\frac{-\omega C R^2}{1 + \omega^2 C^2 R^2} \right] \quad (3.17)$$

Thus the real and imaginary parts of the complex impedance are

$$Z' = \frac{R}{1 + \omega^2 C^2 R^2} \quad (3.18a)$$

$$Z'' = -\frac{\omega C R^2}{1 + \omega^2 C^2 R^2} \quad (3.18b)$$

Eliminating ω from these two equations, Eq. (3.18a) and (3.18b), and rearranging, it follows that

$$Z'^2 + Z''^2 = RZ' \quad (3.19)$$

$$\text{or} \quad \left(Z' - \frac{R}{2} \right)^2 + Z''^2 = \left(\frac{R}{2} \right)^2 \quad (3.20)$$

This is the equation of a circle with radius $R/2$ with its center at $(Z' = R/2, Z'' = 0)$. The coordinates at the top of the arc will be $(R/2, R/2)$. Since $Z' = Z'' = R/2$ at frequency ω_o , Equations (2.18) can be rearranged to give

$$\omega_o RC = 1 \quad (3.21)$$

thus, the impedance response of the resistor in parallel with a capacitor will be a perfect semicircle intersecting the real axis at R and 0 . The relaxation time, $\tau_o = 2\pi RC$, for the circuit is given by the inverse of the frequency at the top of semicircle, ω_o . Therefore the diameter of the circle is the dc resistance of the sample. The impedance plot when they are connected in parallel is shown in Fig. 3.6(a).

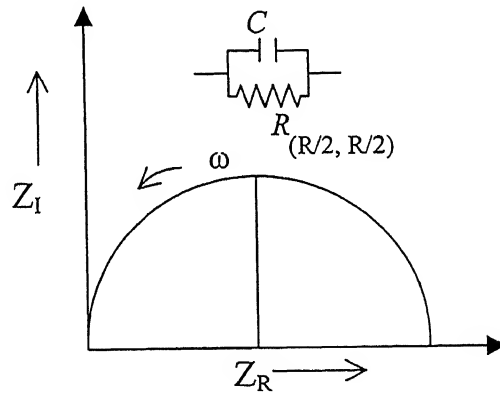


Fig. 3.6(a): Impedance plot for a resistor and a capacitor in parallel

When blocking electrodes are used, an electrode/electrolyte interface capacitance comes into play. This is attributed to the roughness of the electrode-electrolyte interface, the slope of the line decreasing with increasing roughness and a 90° angle of inclination is obtained only for perfectly flat surfaces as shown in Fig. 3.6(b). This type of frequency response can be represented by a constant phase element (CPE) which

has an impedance $Z = A(j2\pi f)^{-n}$, where n has a value between 0 and 1 and A is a constant.

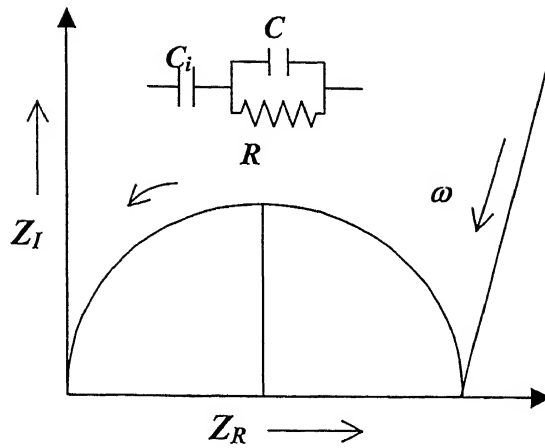


Fig. 3.6(b): Effect of interface capacitance C_i on impedance of electrolyte

In polycrystalline materials, there may be a contribution to the impedance due to the presence of grain boundaries. The grain boundaries may act as a hindrance to the ion transport, but they might also provide a high conductivity path since the defect density may be larger in the interface region. In the first case one can, in some cases detect a second semicircle in the impedance plot representing grain boundaries^[44,45]. The bulk resistance in such a case is obtained from the intersection of the high frequency impedance semicircle [Fig. 3.6(c)] with the real axis. If we have an increased conductivity at the grain boundaries it will give an apparent bulk resistance that is lower than the real bulk effect. A study of the conductivity dependence on grain size may help identify the conductivity mechanism if single crystals are not available. Another common impedance behavior is one in

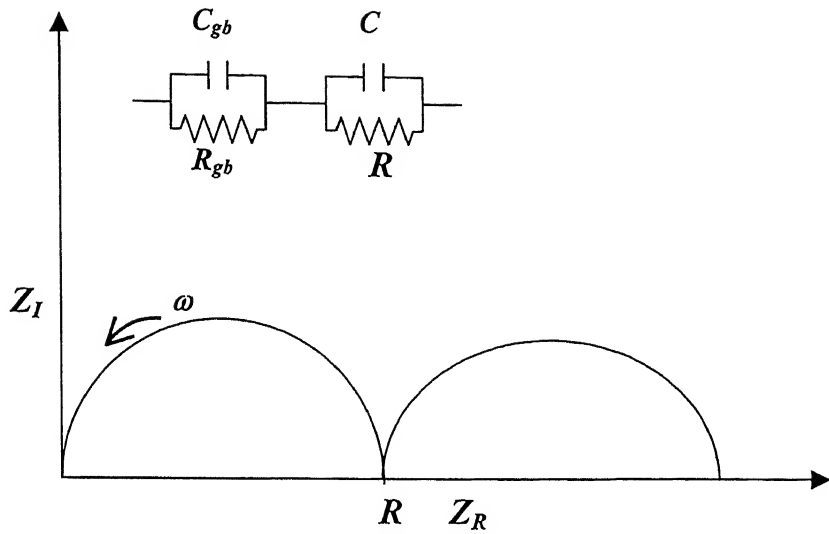


Fig. 3.6(c): Effect of grain boundaries on the impedance of electrolyte

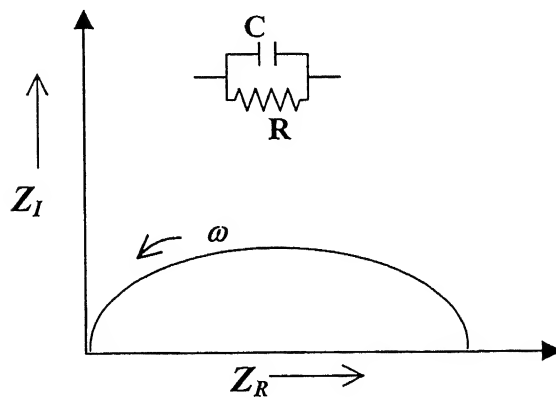


Fig. 3.6(d): Depression of semicircle due to multiple polarizations

which the high frequency semicircle portion of the plot is depressed so that the center of the circle is situated below the real axis [Fig. 3.6(d)]. It has been shown that in this case a CPE connected in parallel with the bulk resistance will result in such a depressed semicircle^[46,47].

3.6 Impedance Measurement Methodology

The impedance measurements for all compositions were carried out using HP4192A impedance analyzer. The sample made in the form of pellet is loaded in the furnace using a specially designed sample holder. Now spot frequency (f) was swept from 1 kHz to 13 MHz for a fixed temperature and values of Z, θ have been noted down. Impedance plots (Z'' vs. Z') have been drawn using the Microcal Origin 6.0 software to ensure that proper points are available. The DC resistance (R_{dc}) have been calculated wherever circular plots are available. The diameter of the semicircle has been considered as R_{dc} . Using this R_{dc} one can calculate the DC conductivity (σ_{dc}) using the equation below:

$$\sigma^* = \frac{l}{R_{dc} A} \quad (3.22)$$

Wherever impedance plots are not coming in circular fashion, $\frac{Z}{\cos\theta}$ at 10 kHz has been used as R_{dc} . This can be explaining further as follows:

The conductivity can be given as,

$$\sigma^* = \frac{l}{Z^* A} \quad (3.23)$$

$$= \frac{l}{(Z' + Z'')A} \quad (3.24)$$

$$= \frac{l}{(Z'^2 + Z''^2)A} (Z' - jZ'') \quad (3.25)$$

Therefore the real part of the conductivity (σ_R or σ_{dc}) can be given as

$$\sigma_{dc} = \frac{l}{(Z'^2 + Z''^2)A} Z' \quad (3.26)$$

$$= \frac{l}{(Z^2)A} Z' \quad (3.27)$$

$$= \frac{l}{Z^2 A} Z \cos \theta \quad (3.28)$$

$$= \frac{l \cos \theta}{ZA} \quad (3.29)$$

$$= \frac{l}{Z/\cos \theta \cdot A} \quad (3.30)$$

Therefore $Z/\cos \theta$ can be used in place of R_{dc} .

Figure 3.7 portraits impedance plots for KCl + 20m/o KI at four different temperatures for a range of frequencies from 1kHz to 13 MHz. The impedance plot consists of $|Z \cos \theta|$ along x-axis and the $|Z \sin \theta|$ along y-axis. The diameter of each plot gives the DC resistance of the sample under study. From this the DC conductivity can be calculated using Eq. (3.22). It can also be seen that the semicircles are depressed and the center does not lie on the real axis. Further as temperature increases, the diameter of the semicircle decreases.

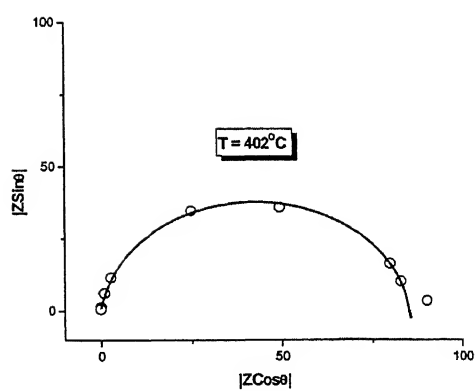
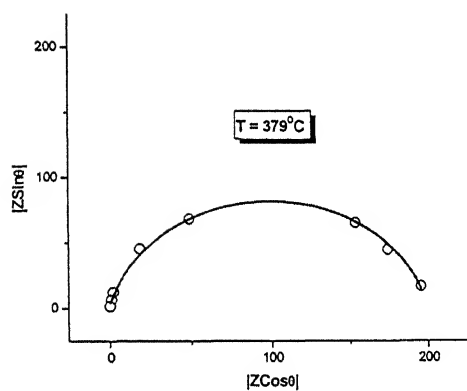
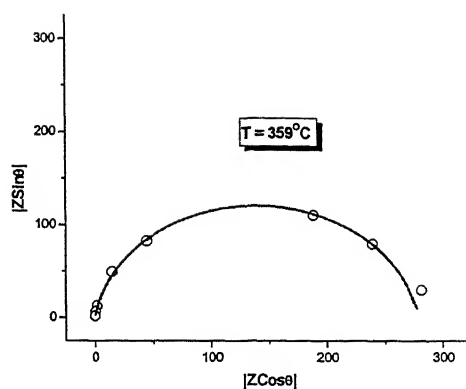
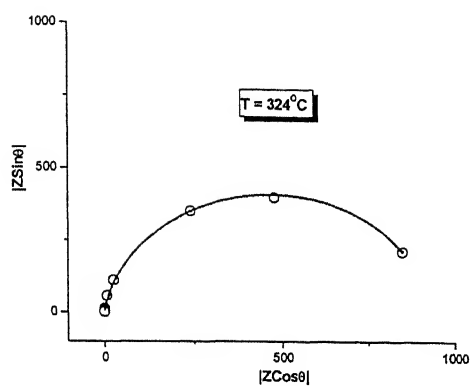


Fig. 3.7: Impedance plots for $\text{KCl} + 20\text{m/o KI}$ at four different temperatures.

3.7 Materials Processing

The starting materials were KCl and KI. These two alkali halides are highly hygroscopic (which can be concluded from FT-IR results discussed in Chapter 4). The physical properties of the materials used are given in Table 3.2.

Table 3.2 The Physical Properties of the Starting Materials

Material	KCl	KI
Source	Aldrich Chemical Comp., USA	Ranbaxy, India
Purity	99+%	99.8%
Molecular Weight	74.56	166.01
Density (gm/cc)	1.984	3.13
Melting point (K)	1043	954
Boiling Point (K)	1773	1603

3.8 Sample Preparation

All the samples have been prepared by melting the stoichiometric mixtures inside a furnace. The starting materials KCl and KI before use were dried in an oven at around 100°C to prevent the samples from absorbing moisture as both the constituting materials are highly hygroscopic. The mixed crystals of different compositions were prepared by weighing appropriate amount of materials in an electronic balance. The transfer of material from oven to the electronic balance was done using a moist-proof desiccator. The starting powders were always carried inside the desiccator whenever needed to minimize the chance of

moisture absorption as much as possible. After weighing, the powders were again kept inside the oven. The mixed powders were then transferred to pre-heated quartz tubes very carefully to avoid loss of powder during transfer. These quartz tubes were placed on a specially grooved ceramic block having 5 grooves for placing the quartz tubes in order to prevent accidental toppling of the tubes as the internal surface of the furnace is cylindrical in shape. The ceramic block along with the quartz tubes was immediately shifted to a furnace pre-heated to 200°C . The temperature of the furnace was raised above the melting point of either starting materials (in this case melting point of pure KCl is 770°C , and the temperature was kept well above 770°C , nearly 850°C). After allowing the melt to remain at this temperature for a few hours (4-5 hrs) for complete homogenization of the two component powders, the furnace was switched off. The melt, in this way, was allowed to cool slowly inside the furnace. Some samples were also quenched. In this case the melt was directly taken outside the furnace and kept in air for cooling. So “furnace-cooled” and “air-cooled” samples were prepared in this way. The re-solidified material was then removed from the quartz tubes carefully and transferred to a pre-heated mortar for grinding in order to get homogenized powder. A high carbon steel die was also pre-heated and a small amount of the melted powder was poured into it. The steel die had 11mm internal diameter. The die was then placed over a hydrostatic press. A force of 4 tons was applied on each sample. The resulting pellets were placed in aluminum crucibles, which are then loaded in a furnace for sintering. All samples were sintered for 10-12 hours in an automated furnace. The rate of heating and cooling was kept at $1.5^{\circ}\text{C/minute}$. The sintered samples were then coated with graphite

paint, which will act as the electrodes for the conductivity experiments. The resistance of the flat surfaces of the pellets after coating with graphite paint was kept at nearly 50Ω . The samples were kept for drying in an oven at 100°C . The pellet was loaded in the sample holder that was equipped with chromel alumel thermocouple to measure the temperature of the sample. The impedance measurements were carried out using HP 4192A impedance analyzer.

Table 3.3 Sintering temperature, sintering time and thickness of different samples prepared (Pelletization pressure 4.0 tons/cm^2).

Composition	Sintering temperature ($^{\circ}\text{C}$)	Time (hrs)	Thickness of the pellet (cm)
KCl	530	10	0.383
KCl + 5m/o KI	490	10	0.513
KCl + 10m/o KI	490	10	0.275
KCl + 15m/o KI	490	10	0.461
KCl + 20m/o KI	490	10	0.329
KCl + 25m/o KI	490	10	0.332
KCl + 30m/o KI	490	10	0.321
KCl + 40m/o KI	490	10	0.338
KCl + 50m/o KI	490	10	0.373
KCl + 60m/o KI	490	10	0.303
KCl + 70m/o KI	490	10	0.305
KCl + 80m/o KI	490	10	0.212
KCl + 90m/o KI	490	10	0.385
KI	490	10	0.345

Chapter 4

Results & Discussion

This chapter deals with the experimental results, mainly the electrical conductivity of KCl-KI mixed crystals as function of temperature and composition. Besides XRD analysis has also been carried out to obtain the structural information for different mixed crystals. BET measurements have been included for analyzing the surface area, which help understand the quality of interfacial contact. Efforts were made to find out the chemical compositions of all the mixed crystals by FT-IR analysis though it did not produce any conclusive results because of the inherent difficulties with halides as they are not so much IR sensitive.

As pointed out earlier, the aim was primarily to examine the effect of “wrong-size” substitutions on the electrical conductivity and also to test the “Lattice Loosening” (LL) model. The percolation model and the $CB\Omega$ model have also been discussed for completeness of this work. Fourteen different compositions of KCl-KI mixed crystals [denoted by $KCl_{1-x}I_x$ where $x = 0, 0.05, 0.1, 0.15, 0.2, 0.25, 0.3, 0.4, 0.5, 0.6, 0.7, 0.8, 0.9, 1.0$] were prepared by melting and re-solidification in air. The XRD results are presented first followed by the BET and the FT-IR results. The conductivity data obtained from the Complex Impedance Analysis (CIA) have been discussed thereafter. The results have been analyzed in the light of existing available

models (i.e., LL model along with the percolation and CBO model) in the discussion section. The chapter finishes with a brief conclusion.

4.1 X-ray Diffraction

The XRD patterns of all the compositions have been shown in Fig. 4.1(a) on a single graph. Figs. 4.1(b) to 4.1(e) show XRD patterns for individual compositions separately. Table 4.1 summarizes the lattice constants of different compositions. The lattice constants have been obtained from XRD analysis and the calculations have been performed considering all the peaks corresponding to KI and KCl separately and then averaging the values for each case.

From Figs. 4.1(a) to Fig. 4.1(e), it is quite obvious that the compositions KCl + xKI ($x \leq 0.7$) show peaks corresponding to both KCl and KI with slight variations in the intensities. However, for the compositions containing more than 70 m/o KI, the KCl peaks have disappeared. This suggests that at room temperature, KCl containing more than 70 m/o KI constitutes solid solution which is consistent with the available phase diagram^[40] of KCl-KI system (Fig. 4.2). The demixing curve has been shown in the phase diagram, which separates the two-phase region ($\alpha + \beta$) from the solid solution (SS) region. Therefore it can be concluded that a maximum 30 m/o KCl goes into solid solution with KI. The phase diagram also depicts that at lower concentrations of KI ($x \leq 0.08$) there is a possibility of formation of solid solution. But our XRD results do not support this fact as both the peaks of KCl and KI are present in the system containing less than 8 m/o KI.

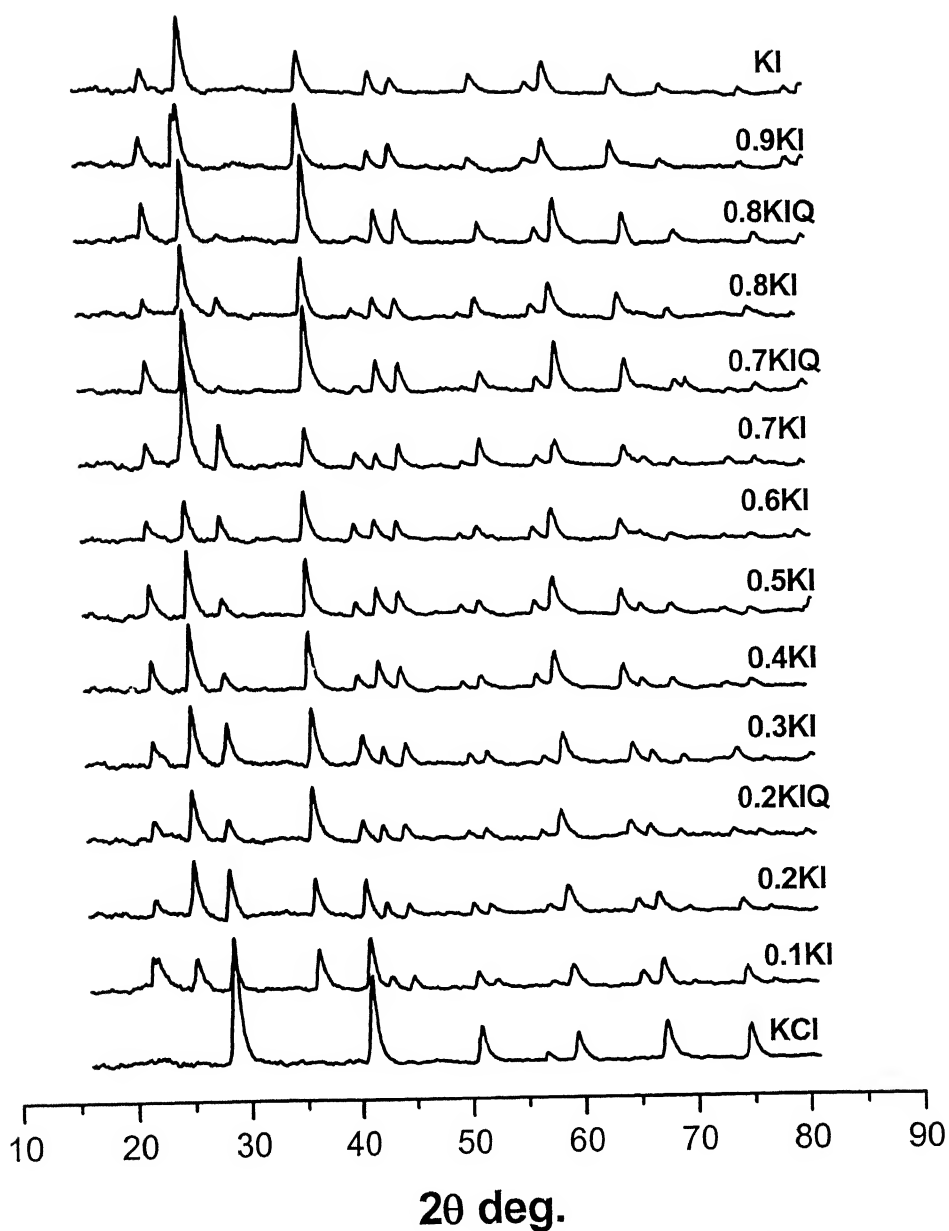


Fig. 4.1(a): XRD plots for various compositions. Here $\text{KCl} + x\text{KI}$ ($0 < x < 1.0$) has been denoted as only $x\text{KI}$. 'Q' stands for quenched samples.

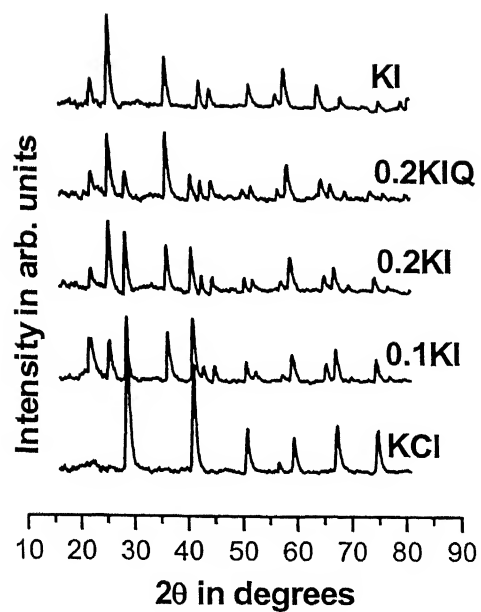


Fig.4.1(b)

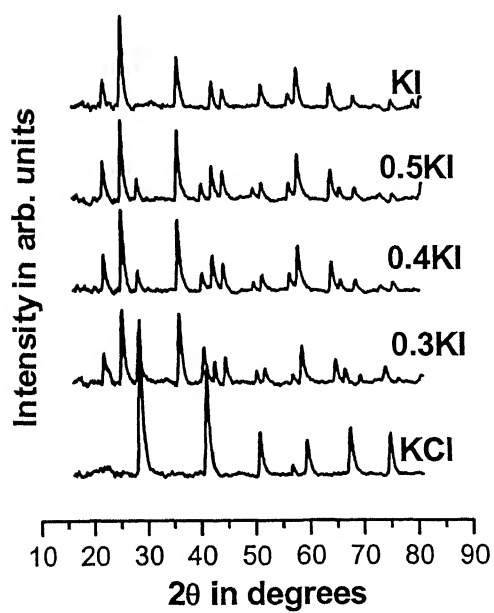


Fig. 4.1(c)

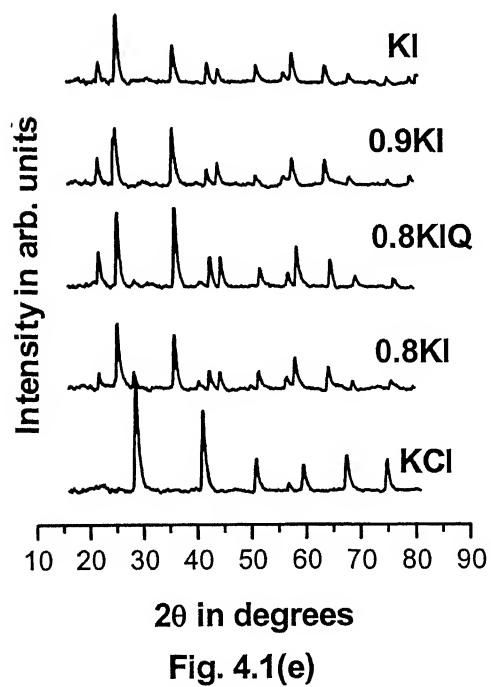
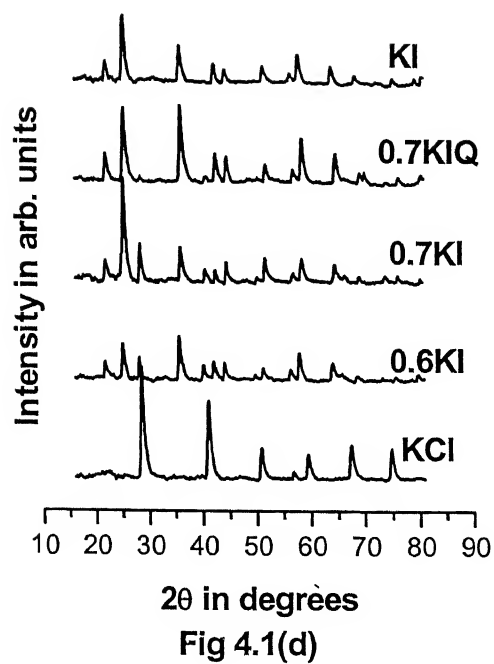


Fig. 4.1(b)-(e): Different XRD patterns for various compositions of KCl-KI system. Here 'Q' stands for quenched samples.

This discrepancy can be attributed to the fact that the XRD measurements have been carried out at room temperature whereas the available phase diagram shows informations only above 400°C . The phase diagram is too old (1912) and there may be variations in the concentration of impurities already present in the original sample. Moreover additional peaks may appear because of the hydrate formation as the constituting powders are very hygroscopic which has been confirmed from the FT-IR studies for the presence of the OH^- group. At lower concentrations some peaks may disappear also because of less amount of dopant present.

One interesting finding is that in quenched $\text{KCl} + 70 \text{ m/o KI}$ sample the KCl peaks have disappeared [Fig. 4.1(d)] whereas in the case of furnace cooled sample of the same composition, the KCl peaks are present. The observation in the case of $\text{KCl} + 20 \text{ m/o KI}$ is different. Here the quenched sample [Fig. 4.1(b)] does not form solid solution as peaks corresponding to both KCl and KI are present. This supports the general fact that a larger ion (I^- in this case) is more accommodating than a smaller ion owing to its high polarizability. Therefore the XRD analysis suggests a limited solid solubility of KI in KCl and vice versa at room temperature.

It is also evident from the XRD results that there is a shift in the position of the peaks corresponding to pure KCl towards lower 2θ values. This suggests that the lattice parameter has increased according to the Bragg's law. From Table 4.1 it can be seen that the lattice constant of KCl increases slightly due to the substitution of larger I^- ions. For example the lattice constant of $\text{KCl} + x\text{KI}$ is $\sim 6.2 \text{ \AA}$ for $x \leq 0.1$ which increases to 6.3 \AA for $x > 0.1$. The slight increase in lattice constant of KCl may be due to solubility of larger I^- ions

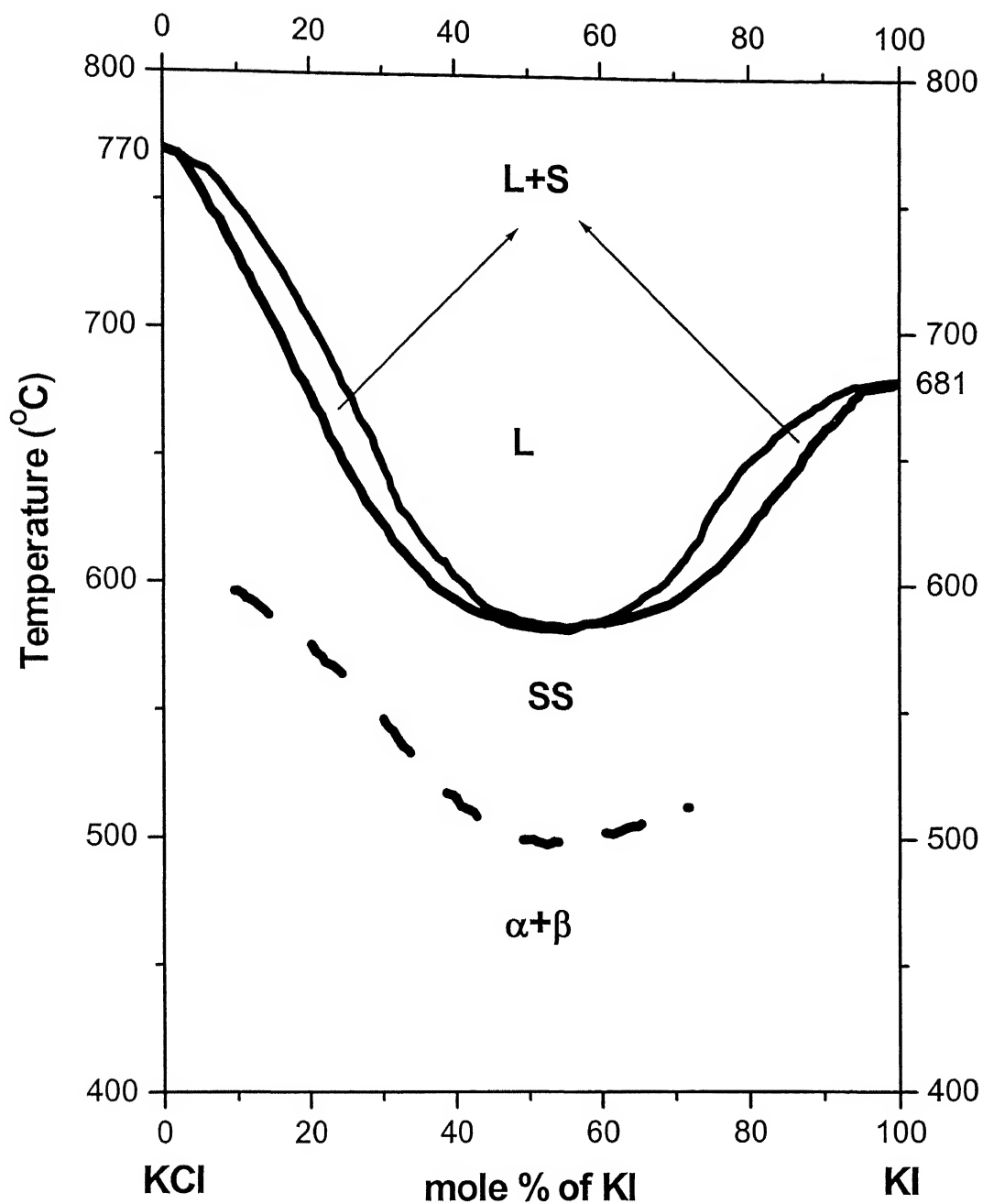


Fig. 4.2: Phase diagram of KCl-KI system re-plotted using the data obtained from literature^[40].

$[r_{\text{cl}} = 1.81 \text{ \AA}; r_{\text{I}} = 2.20 \text{ \AA}]$, which tends to expand the lattice and creates strain in the host lattice. This is expected to increase the concentration of vacancies, according to LL model. The error in measurement of lattice constant in Table 4.1 for pure KCl and pure KI is $\sim 1\%$ and $\sim 0.2\%$ respectively. However, the lattice constant of KI does not exhibit any trend and thus it is difficult to draw any conclusion about the solubility of KCl in KI.

Table 4.1 Lattice constant for different compositions of KCl-KI system

Composition x (KCl + xKI)	Lattice Constant (\AA)	
	KI	KCl
0	-	6.2
0.1	7.04	6.2
0.2	7.04	6.3
0.3	7.05	6.3
0.4	7.10	6.3
0.5	7.10	6.3
0.6	7.12	6.3
0.7	7.08	6.3
0.8	7.09	6.3
0.9	7.12	-
1.0	7.08	-

The crystallite size was also calculated using the available XRD data. The FWHM (full width at half maximum) at appropriate 2θ value was accurately

calculated using PeakFit (V. 4.0) software. The standard sample used was silicon. Crystallite size was calculated using Debye-Scherrer formula

$$t = \frac{0.9\lambda}{B \cos \theta} \quad (4.1)$$

where λ is the wavelength of the x-ray ($\text{CuK}\alpha$) used which is equal to 1.5405 \AA , B is the full width at half maximum (FWHM) after correction from standard sample and θ is the angle corresponding to the peak position. B is given by:

$$B = \sqrt{(B_m^2 - B_s^2)} \quad (4.2)$$

where B_m is the FWHM of the sample whose crystallite size is to be analyzed and B_s is the FWHM of the standard sample (in this case silicon). Each of them are in radians. Table 4.2 gives the crystallite size for different compositions.

Table 4.2 Crystallite size for different compositions.

Sample	Particle Size t (nm)
KCl	38
KCl + 10 m/o KI	47
KCl + 20 m/o KI*	58
KCl + 30 m/o KI	44
KCl + 40 m/o KI	62
KCl + 60 m/o KI	54

Sample	Particle Size t (nm)
KCl + 70 m/o KI	53
KCl + 70 m/o KI*	41
KCl + 80 m/o KI	64
KCl + 80 m/o KI*	53
KCl + 90 m/o KI	54
KI	70

* quenched samples

4.2 BET Measurements

The samples for BET measurements were prepared by thorough grinding of the re-solidified chunk obtained from the melt. The surface area was analyzed by the Coulter SA3100 analyzer, which is based on gas sorption method. The gas used for this purpose was nitrogen. The various parameters involved in BET measurements are listed below in Table 4.3.

Table 4.3 Various quantities involved in BET measurements.

Composition x (KCl + xKI)	Sample Weight (gm)	Elapsed Time (min.)	Outgas Time (min.)	Outgas Temperature (°C)
0.1	0.4315	19	30	120
0.2	0.3994	20	30	120
0.7	0.3184	21	30	120
0.8	0.5651	20	30	120

The specific surface areas from BET measurements for these samples are shown in Table 4.4.

Table 4.4 Specific surface areas of different samples.

Composition x (KCl + xKI)	Specific surface Area (m^2/gm)	Correlation Constant
0.1	0.385	0.744474
0.2	0.447	0.84779
0.7	0.571	0.63374
0.8	0.653	-0.01310

The low value of specific surface area in all these cases indicate the surface contact between the electrolyte and the electrode will be poor which will affect the ionic conductivity results. Moreover higher specific surface area means smaller grain sizes, thus conductivity will increase as smaller grains have more number of grain boundaries and defects, as is expected for KCl + 80 m/o KI (see Section 4.4.2).

4.3 Fourier Transform Infrared Spectroscopy (FT-IR)

The samples were prepared by usual melting, cooling and then grinding in an agate mortar. The FT-IR studies were carried out with a spectrometer model Vector-22 (Bruker) in the range $400-4000\text{ cm}^{-1}$. Measurements were made on amorphous material dispersed in KBr in the ratio 1:30. The FT-IR spectra of some samples have been shown in Fig.4.3. All the FT-IR plots show clearly that a considerable amount of OH^- is present in every sample

as there is a peak near 3440 cm^{-1} . Some more peaks may correspond to the various impurities already present in the samples especially in KI. Table 4.5 lists some of the impurity groups normally present in KI and their corresponding wave numbers.

Table 4.5 Some impurity groups present in KI and their wave numbers.

Impurity Group	Wave Number (cm^{-1})
IO_3^-	730-785
CO_3^{-2}	1410-1450
PO_4^{-3}	1000-1100
SO_4^{-2}	1080-1130

4.4 Complex Impedance Analysis

4.4.1 Conductivity vs. Temperature

Complex Impedance Analysis (CIA) was used to obtain the DC conductivity of each composition at various temperatures. The variation of real and imaginary parts of complex impedance as a function of frequency has been used to calculate the DC resistance. Fig. 4.4 shows the variation of real and imaginary parts of complex impedance as a function of frequency at four different temperatures for $\text{KCl} + 80\text{ m/o KI}$. Similar plots were obtained in case of all samples and at different temperatures. It is evident from Fig. 4.4 that proper semi-circles are obtained within the limits of experimental error. This suggests that the sample/electrode assembly behaves like a parallel combination of resistor and a capacitor. The DC resistance, in this case, is thus given by the diameter of the semi-circle.

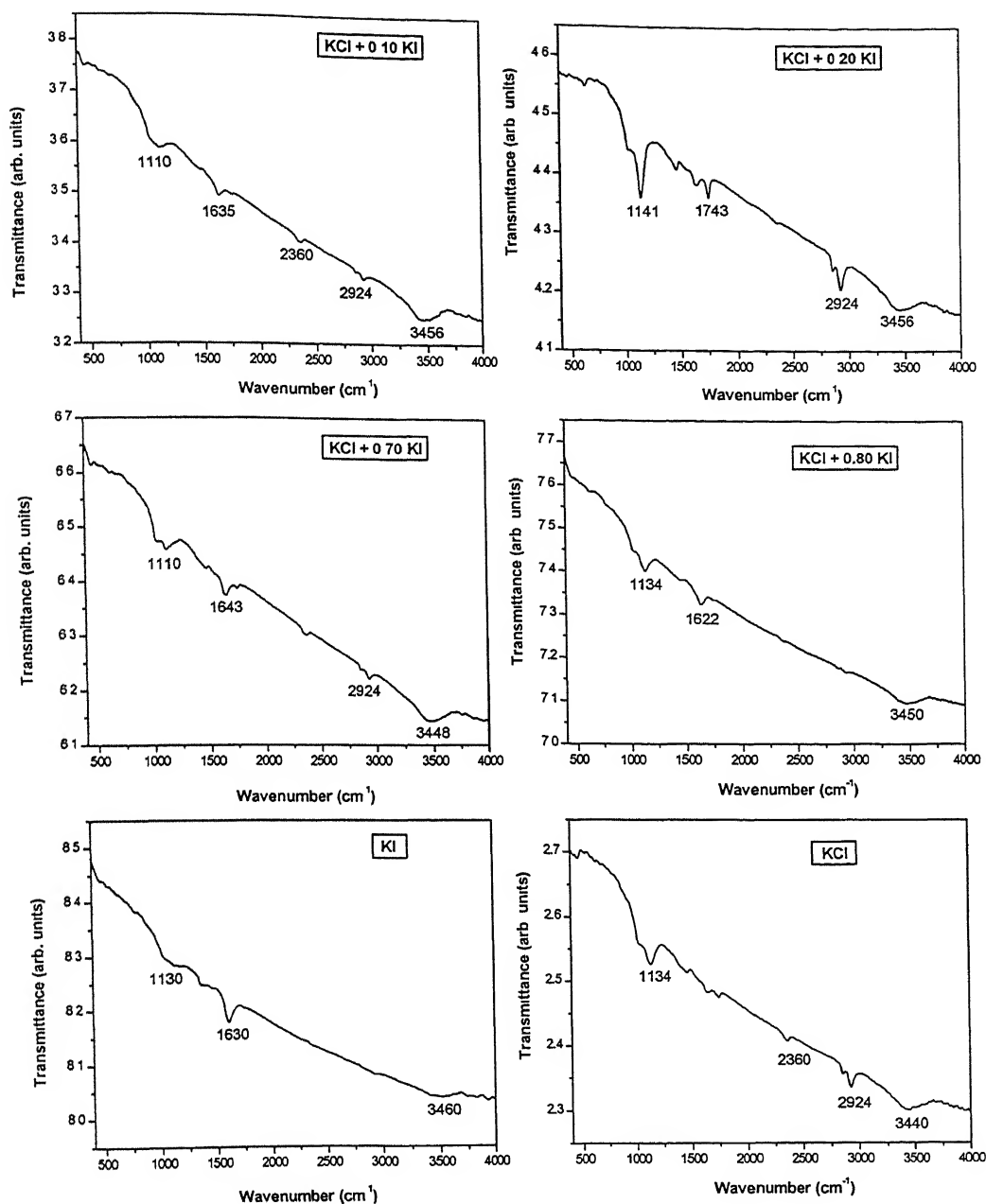


Fig. 4.3: FT-IR Spectroscopy of different compositions of KCl + xKI ($0 < x < 1.0$).

The DC conductivities obtained as described above have been plotted against inverse absolute temperature for all the fourteen samples. Figs. 4.5 [a-j] show some of the typical $\log \sigma_{dc}$ vs. $1/T$ plots. These results are for samples prepared by melting and then cooling them inside the furnace. Some samples have been prepared by cooling them in air or quenching. Fig. 4.6 shows the DC conductivity vs. $1/T$ plot for KCl + 20 m/o KI samples in which one sample has been cooled in air. The ionic transport parameters like knee temperature, extrinsic activation energy and intrinsic activation energy for all the studied compositions are summarized in Table 4.6.

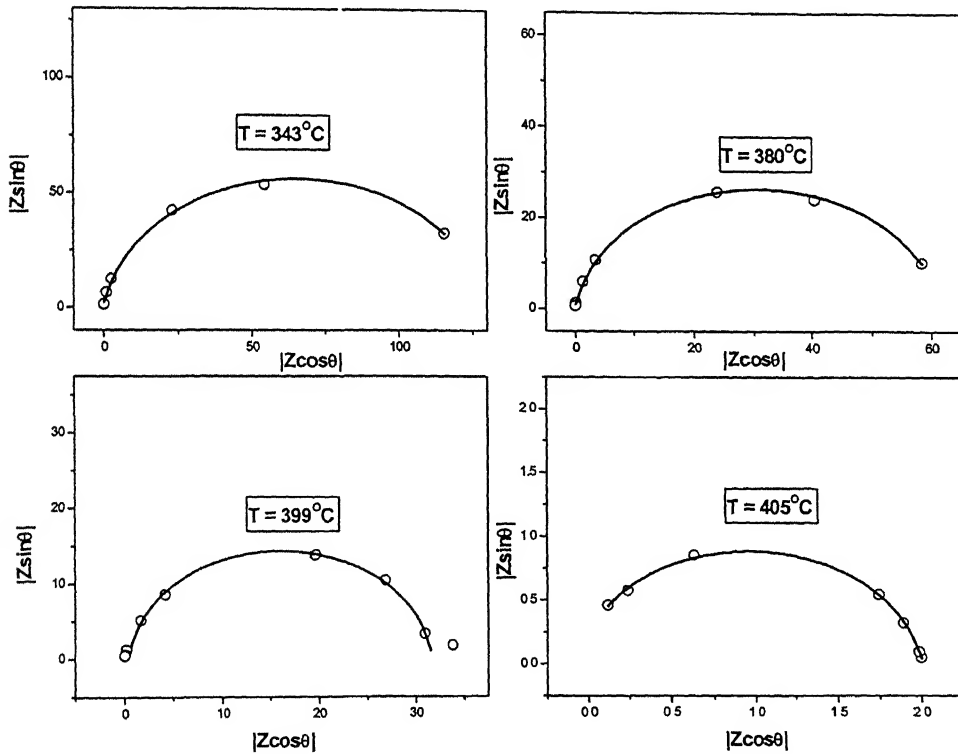


Fig. 4.4: Complex impedance plots for KCl + 80 m/o KI at four different temperatures.

Table 4.6 Various transport parameters of $\text{KCl}_{1-x}\text{I}_x$ system.

Composition	Knee Temperature $T_N (^{\circ}\text{C})$	Activation Energy (eV)	
		Extrinsic	Intrinsic
KCl	604	1.16	2.33
KCl + 5 m/o KI	511	0.63	1.26
KCl + 10 m/o KI	430	0.54	1.34
KCl + 15 m/o KI	390	0.73	1.32
KCl + 20 m/o KI	361	0.68	1.72
KCl + 25 m/o KI	465	1.08	1.28
KCl + 30 m/o KI	379	0.96	1.59
KCl + 40 m/o KI	378	0.59	0.93
KCl + 50 m/o KI	395	0.68	1.31
KCl + 60 m/o KI	416	0.69	1.26
KCl + 70 m/o KI	368	0.71	1.08
KCl + 80 m/o KI	368	0.62	1.34
KCl + 90 m/o KI	375	0.51	0.80
KI ^[32]	465	1.53	1.89

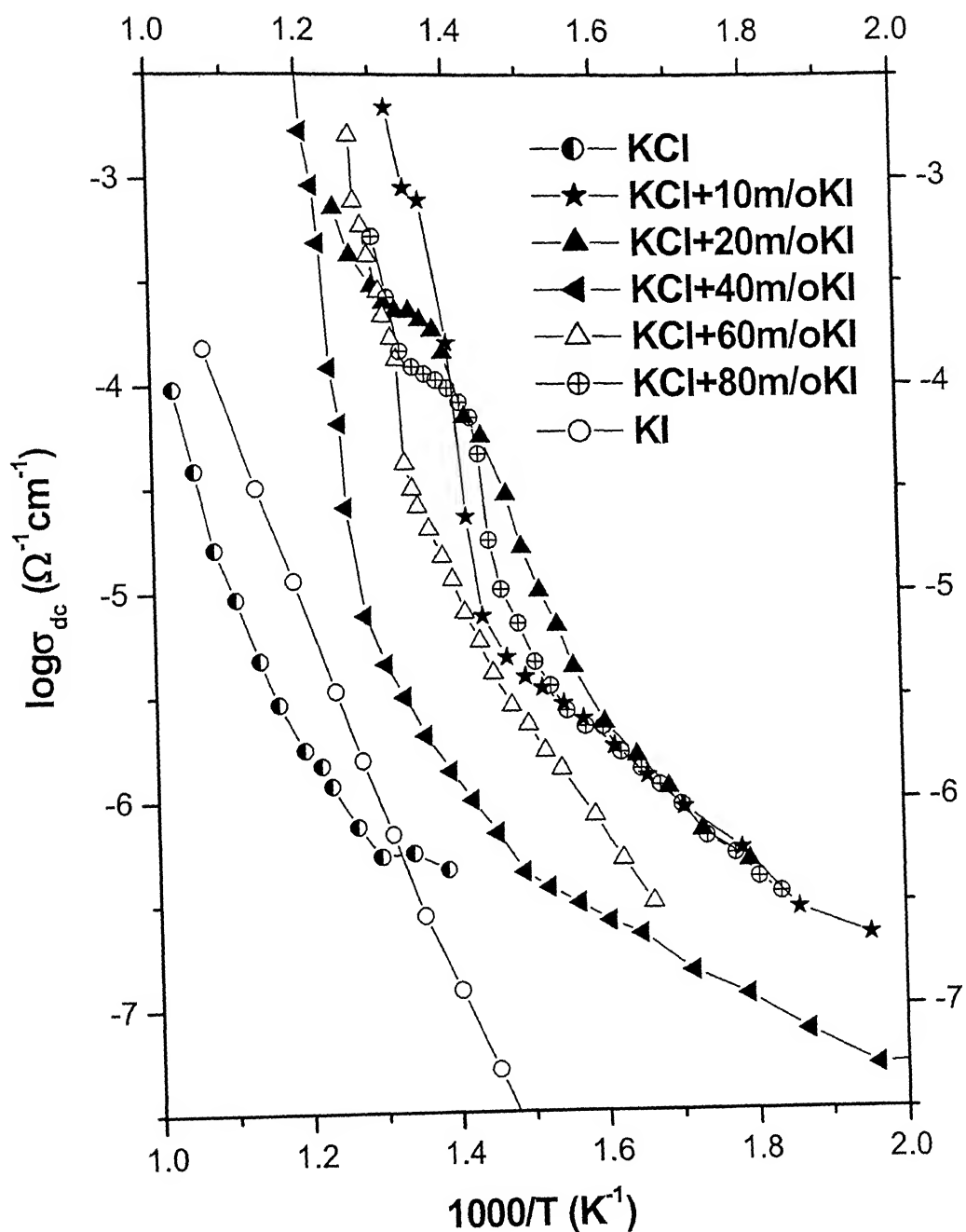
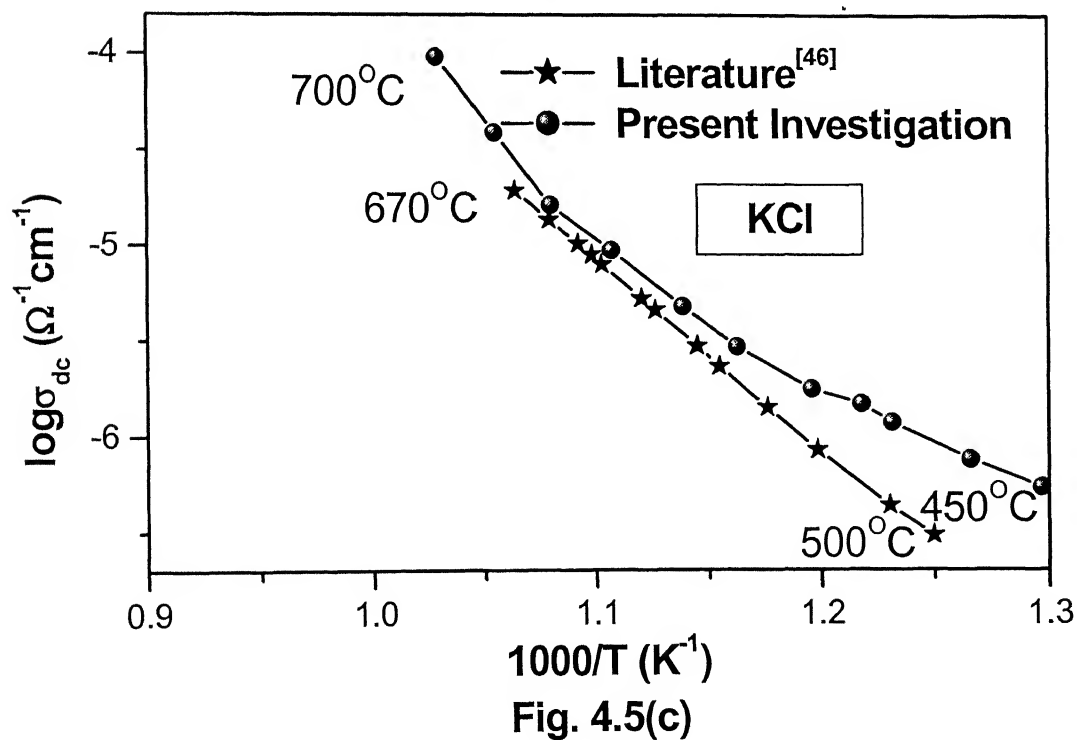
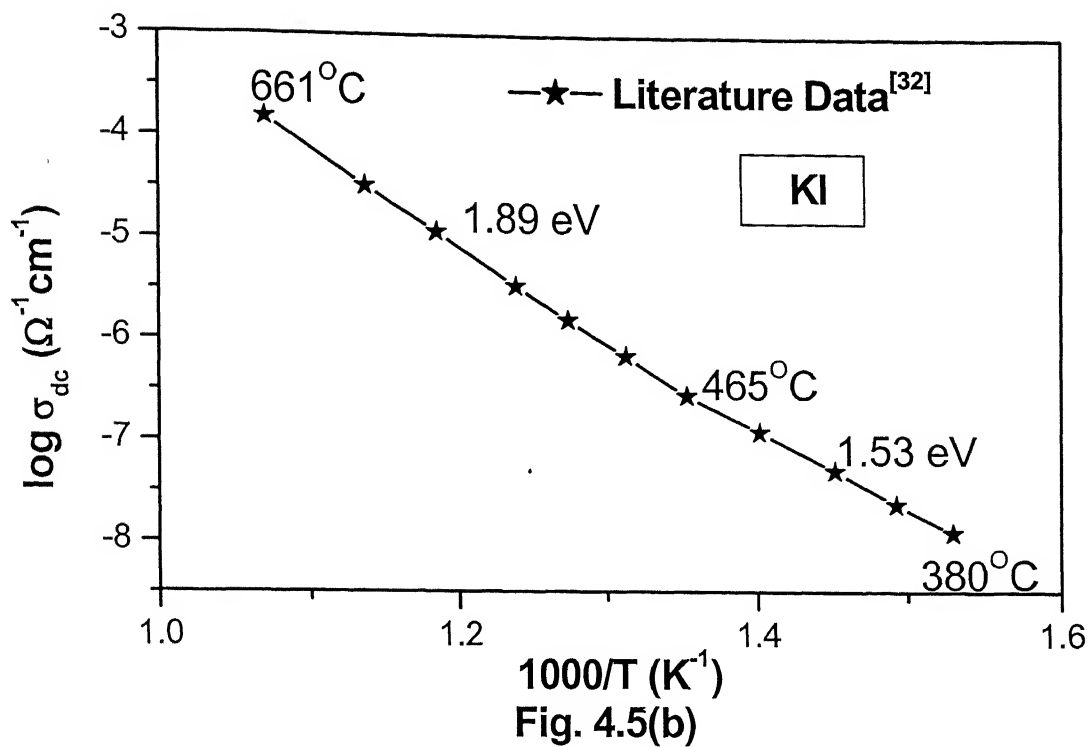


Fig. 4.5(a): Variation of DC conductivity with inverse temperature for different compositions of KCl-KI system.



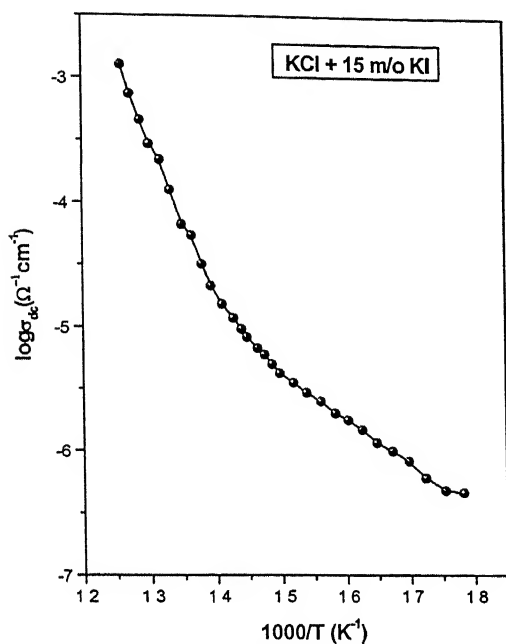


Fig. 4.5(d)

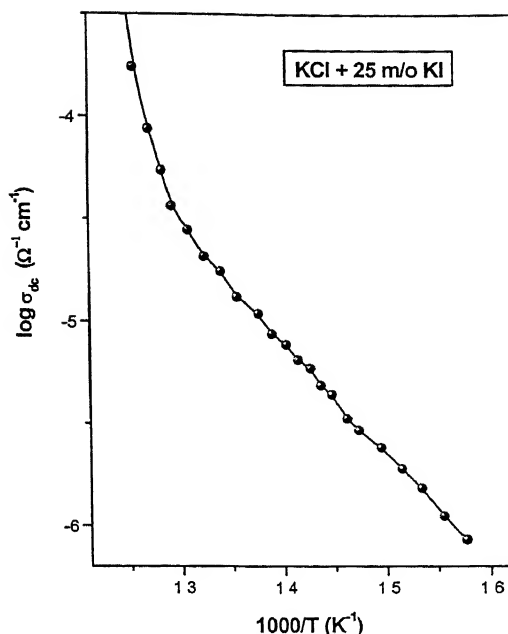


Fig 4.5(e)

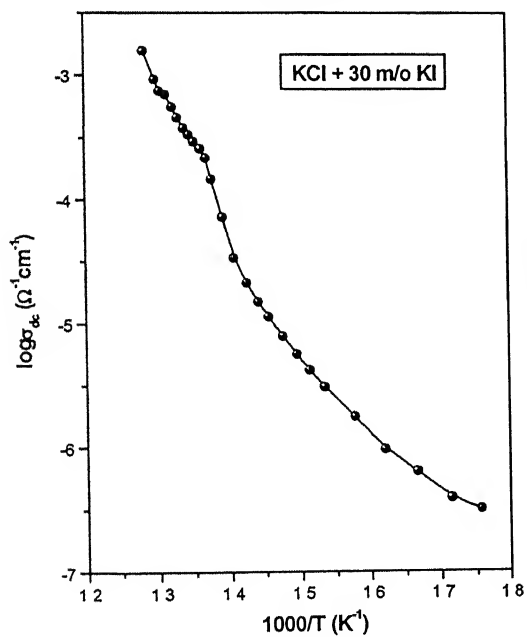


Fig. 4.5(f)

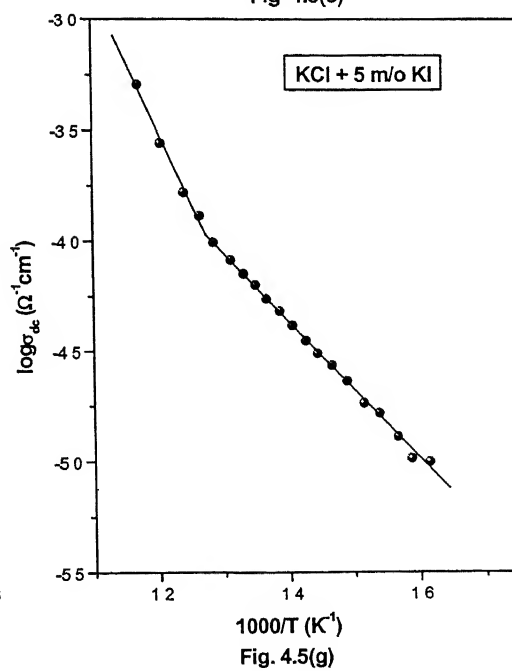


Fig. 4.5(g)

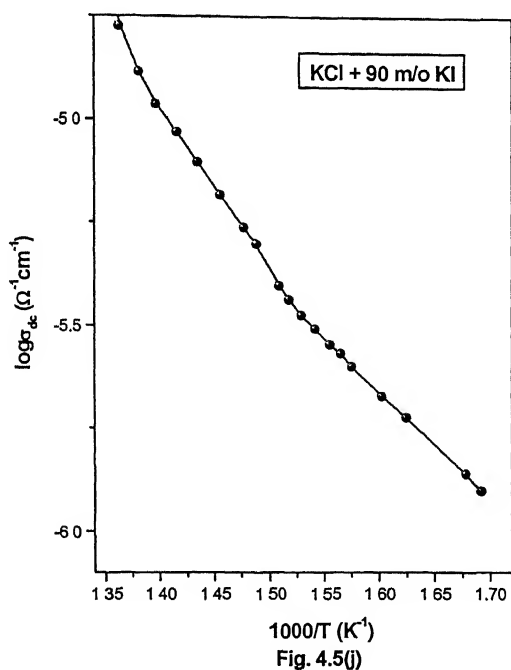
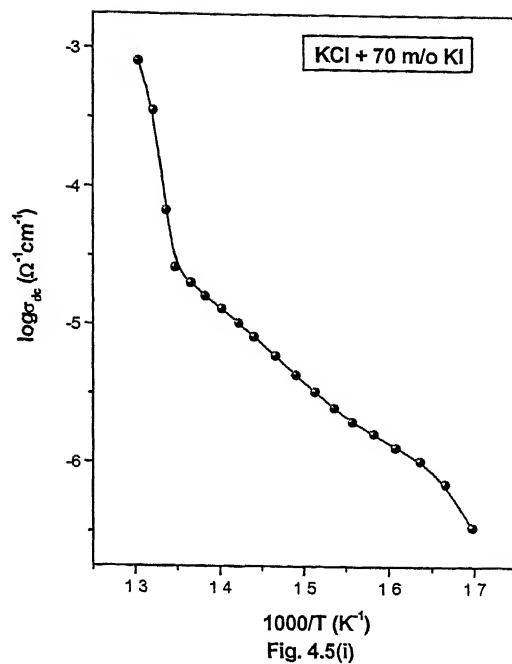
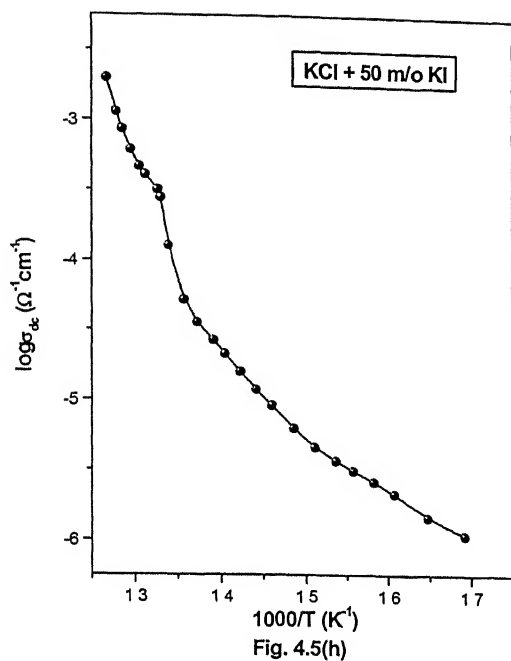


Fig. 4.5(b-j): Conductivity vs. inverse temperature for KCl + x m/o KI ($0 \leq x \leq 100$) system.

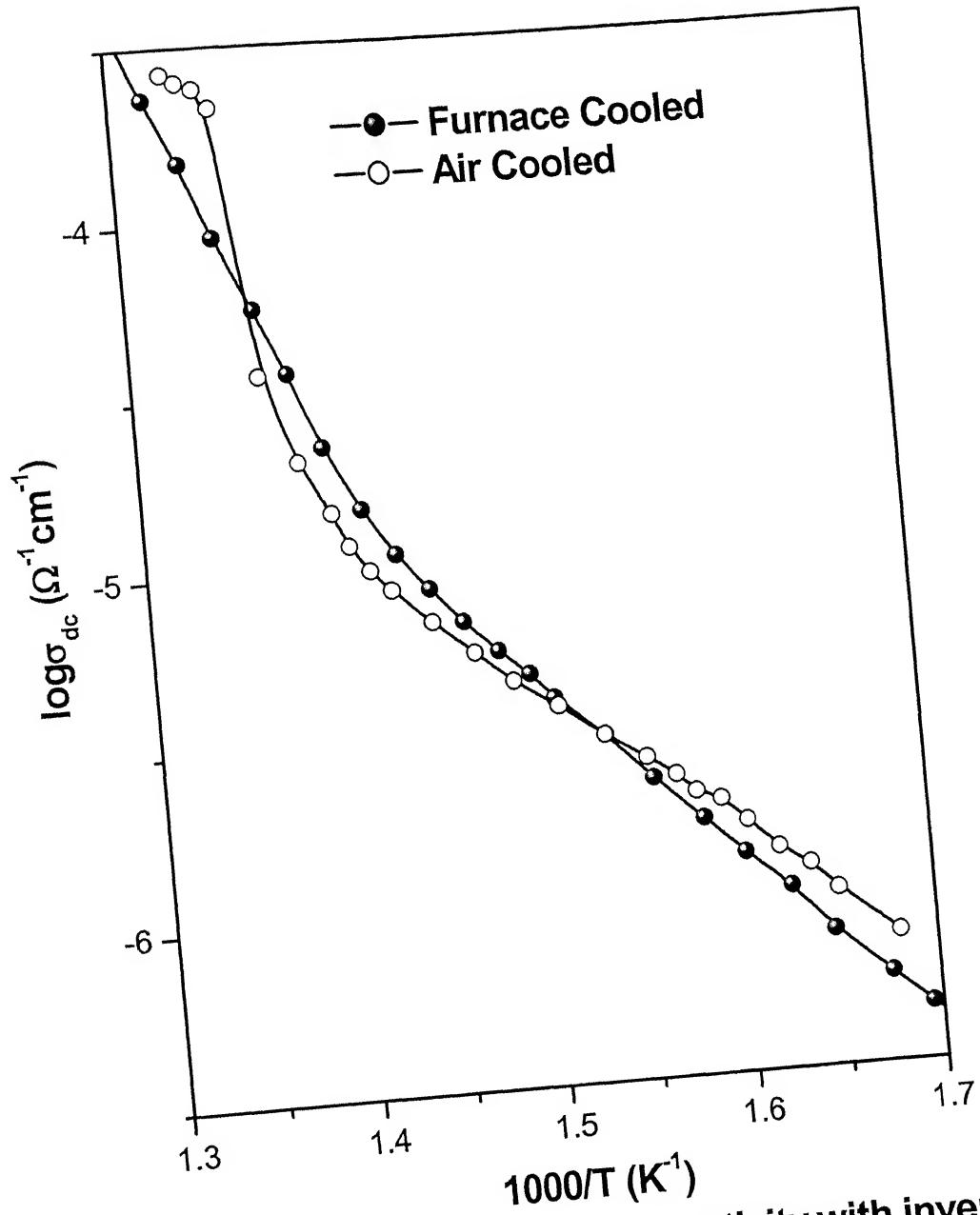


Fig. 4.6: Variation of DC conductivity with inverse temperature for two samples of KCl + 20 m/o KI.

All the plots in Figs. 4.5[a-j] and in Fig. 4.6 show that the logarithm of conductivity varies linearly with inverse of temperature maintaining two distinct slopes in the (low temperature) extrinsic region and the (high temperature) intrinsic region, separated by a knee point T_N . The activation energies in the two temperature regimes have been calculated for all the samples.

In Fig. 4.6 the logarithm of conductivity has been plotted with inverse of temperature for $\text{KCl} + 20 \text{ m/o KI}$ prepared in two different ways. Here one sample has been prepared by quenching and the other by furnace cooling. It is quite obvious that the nature of both the plots is similar and they nearly follow each other from extrinsic to intrinsic region. Normally the quenched samples are supposed to show a higher conductivity due to the creation of larger number of vacancies. But in the present case there is no considerable enhancement in conductivity. This may be due to the fact that the vacancies so formed at high temperature may get annihilated during cooling.

4.4.2 Conductivity vs. Composition

Figure 4.7 shows the DC conductivity obtained from complex impedance analysis as a function of composition at three different temperatures viz. at 355, 400 and at 430°C. These three temperatures have been so chosen that they can show the variation from extrinsic as well as from the intrinsic region as our primary aim is to investigate the enhancement in conductivity due to the substitution of homovalent dopants. It is observed that as the concentration of KI in KCl increases, the ionic conductivity of the system also increases initially, goes through a maximum near to the composition of

$x \approx 0.20$ KI in the two phase region ($0.10 < x < 0.70$), then decreases slowly, attains a local minima at around 0.40 KI and then virtually remains constant for temperatures 355 and 400°C before again passing through a maximum at the composition of ≈ 0.80 KI in the solid solution region. Fig. 4.8 shows the enhancement in conductivity at three different temperatures for all the compositions. It is evident from these two plots that the enhancement in conductivity is more prominent at higher temperatures. In the solid solution region, i.e., for $0.1 > x > 0.7$, the conductivity at 430°C passes through a maximum between two minima at $x = 0.7$ and $x = 1.0$. Therefore it is observed that the conductivity has two local maxima (one in two phase region and the other in solid solution region) and between these two maxima the conductivity does not vary significantly. It is interesting to note that as soon as the solid solution domain is reached the conductivity starts shooting up and reaches a maximum and then decreases subsequently. Table 4.7 summarizes the magnitude of conductivity and the enhancement in conductivity for three compositions at three different temperatures obtained from Fig. 4.7 and Fig. 4.8.

4.4.3 Activation Energy & Knee Temperature vs. Composition

The variation of activation energy (h_m and E_a) and the knee temperature (T_N) as a function of composition are shown in Figs. 4.9, 4.10 and 4.11 respectively. In all these plots the logarithm of conductivity ($\log \sigma_{dc}$) has also been included on the other ordinate for correlation. It is easily confirmed that while the conductivity increases due to the substitution of homovalent dopants the activation energies corresponding to extrinsic and intrinsic

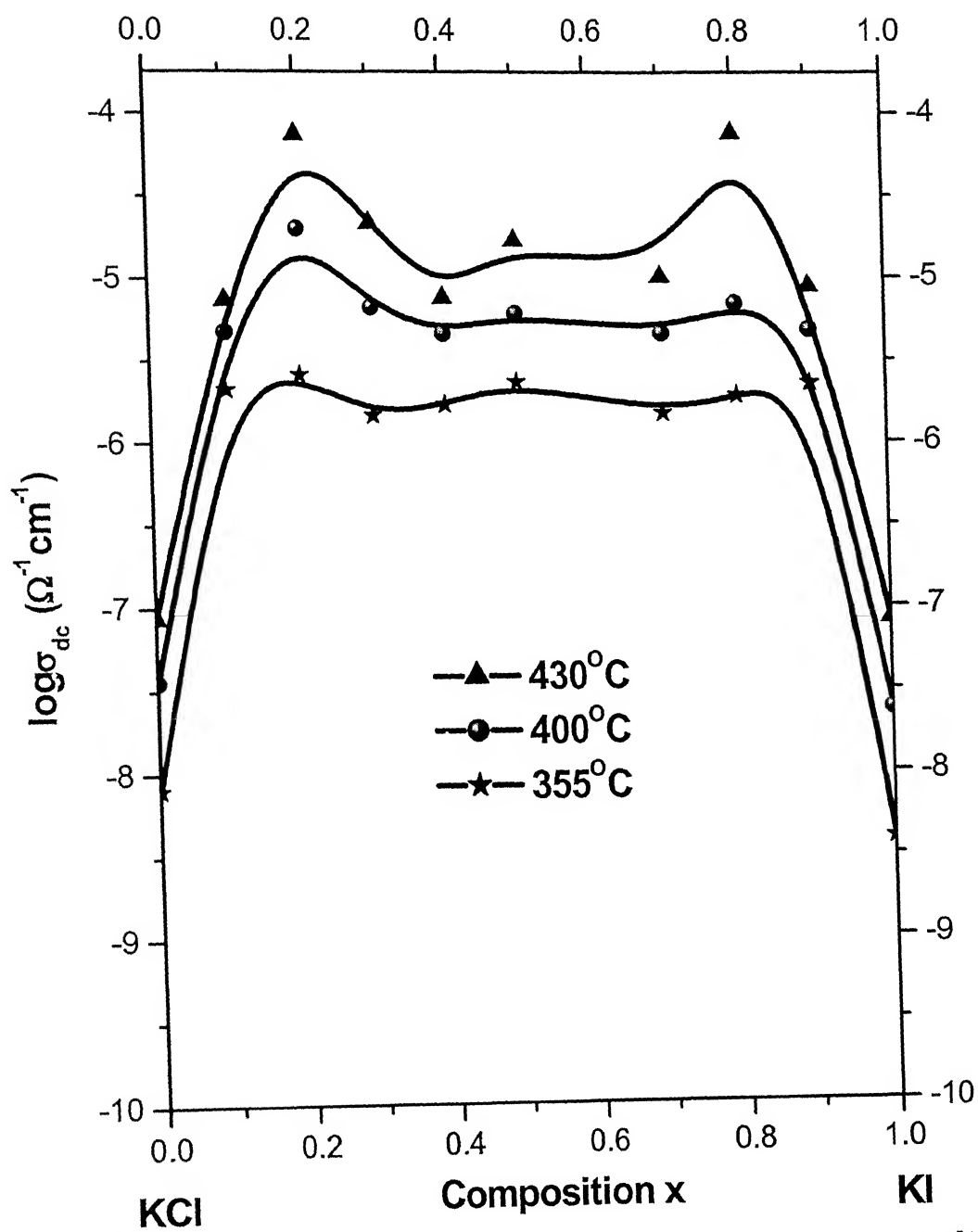


Fig. 4.7: Variation of DC conductivity with composition at three different temperatures for KCl + xKI ($0 < x < 1$).

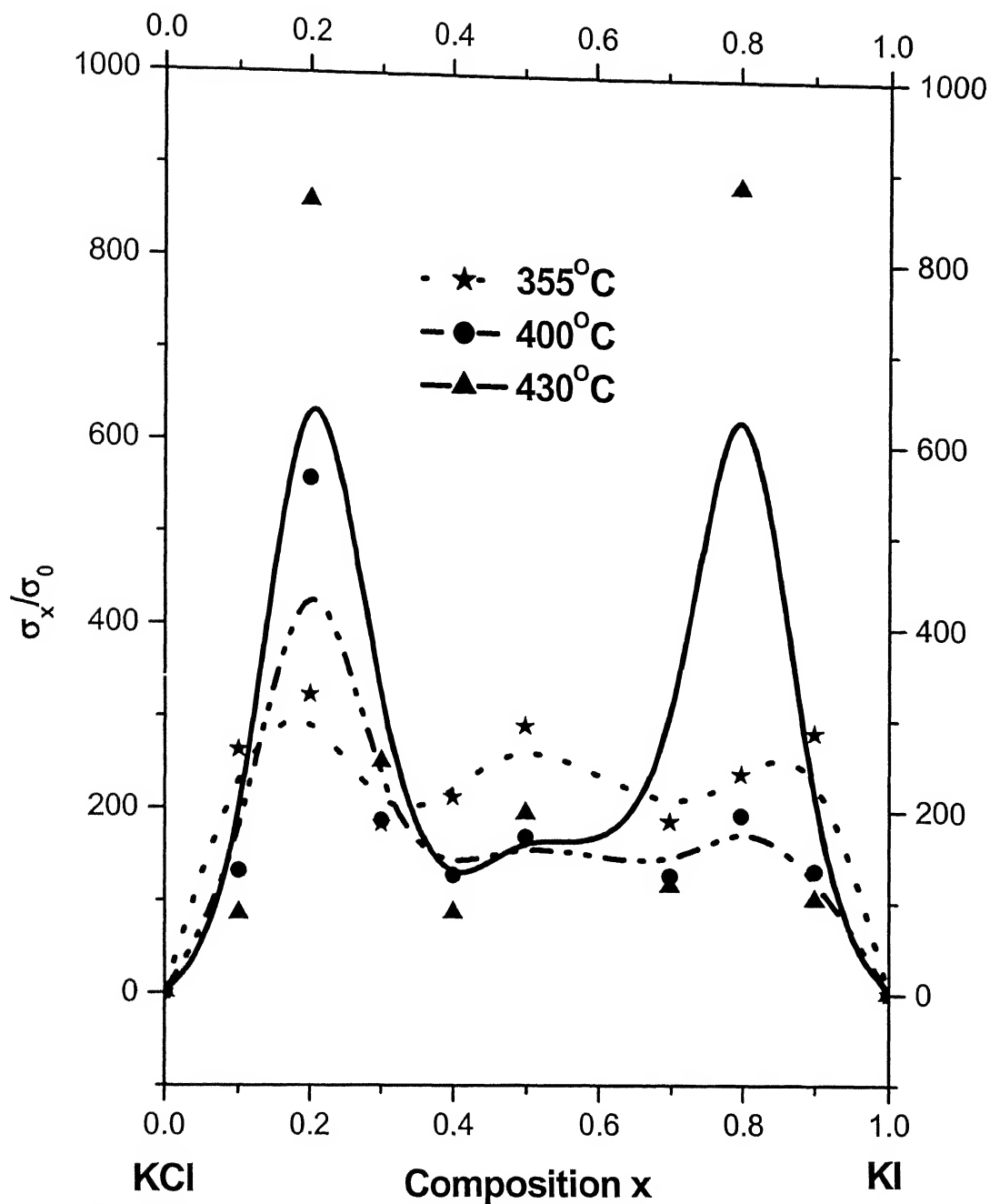


Fig 4.8: Relative conductivity (σ_x/σ_0) as a function of composition at three different temperatures.

Table 4.7 Magnitude of conductivity and enhancement factor for three compositions at three different temperatures of KCl-KI system.

Composition x (KCl + xKI)	Temperature $T (^{\circ}C)$	σ_x at $T^{\circ}C$ ($\times 10^{-6} \Omega^{-1} cm^{-1}$)	σ_x/σ_0 at $T^{\circ}C$
0.2	355	2.6	294
	400	20.0	430
	430	74.1	634
0.8	355	1.9	241
	400	7.0	169
	430	76.0	624
0.9	355	2.3	235
	400	4.8	127
	430	8.9	233

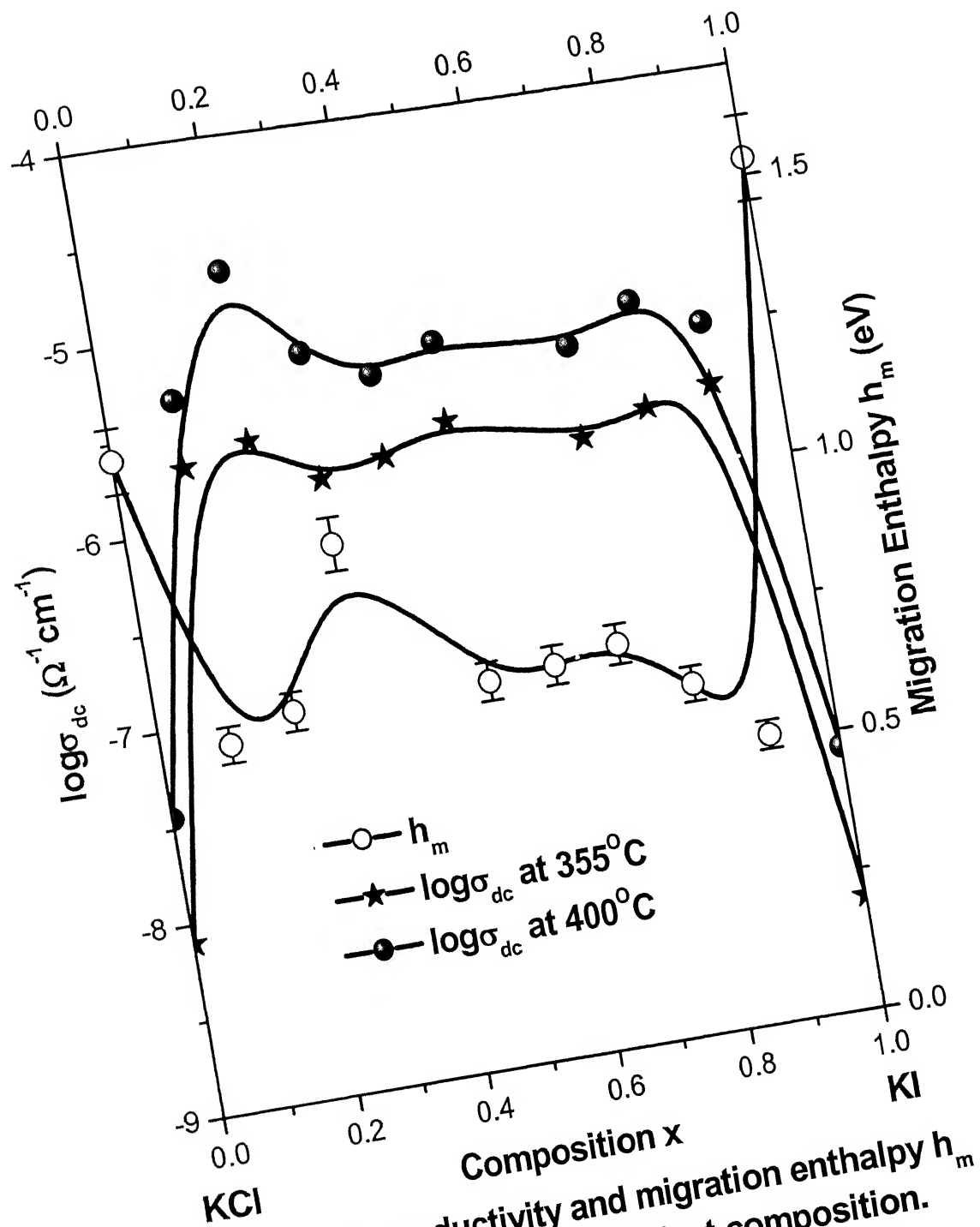


Fig. 4.9: DC conductivity and migration enthalpy h_m plotted on the same graph against composition.

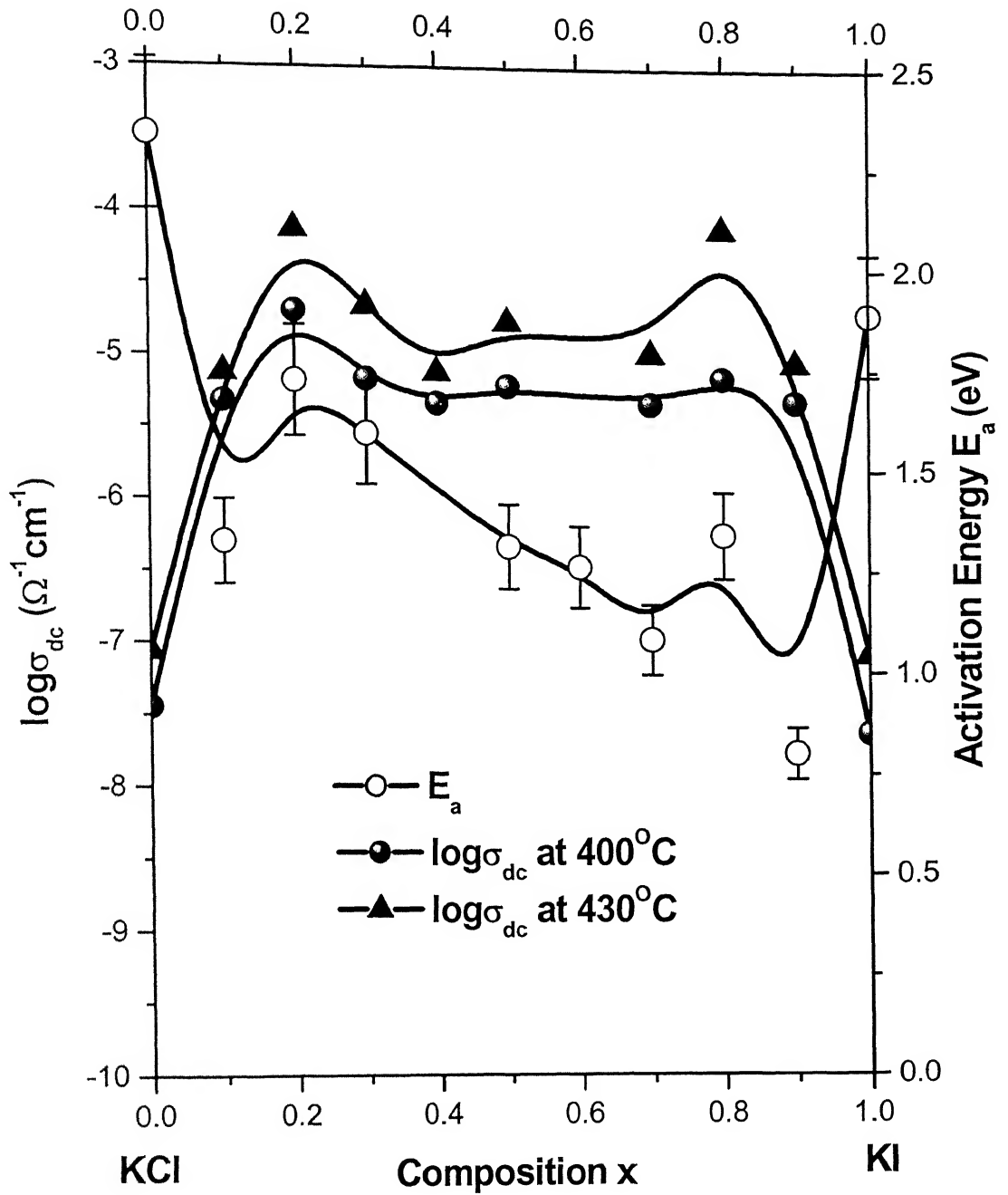


Fig. 4.10: Conductivity and activation energy E_a of intrinsic region plotted on the same graph against composition.

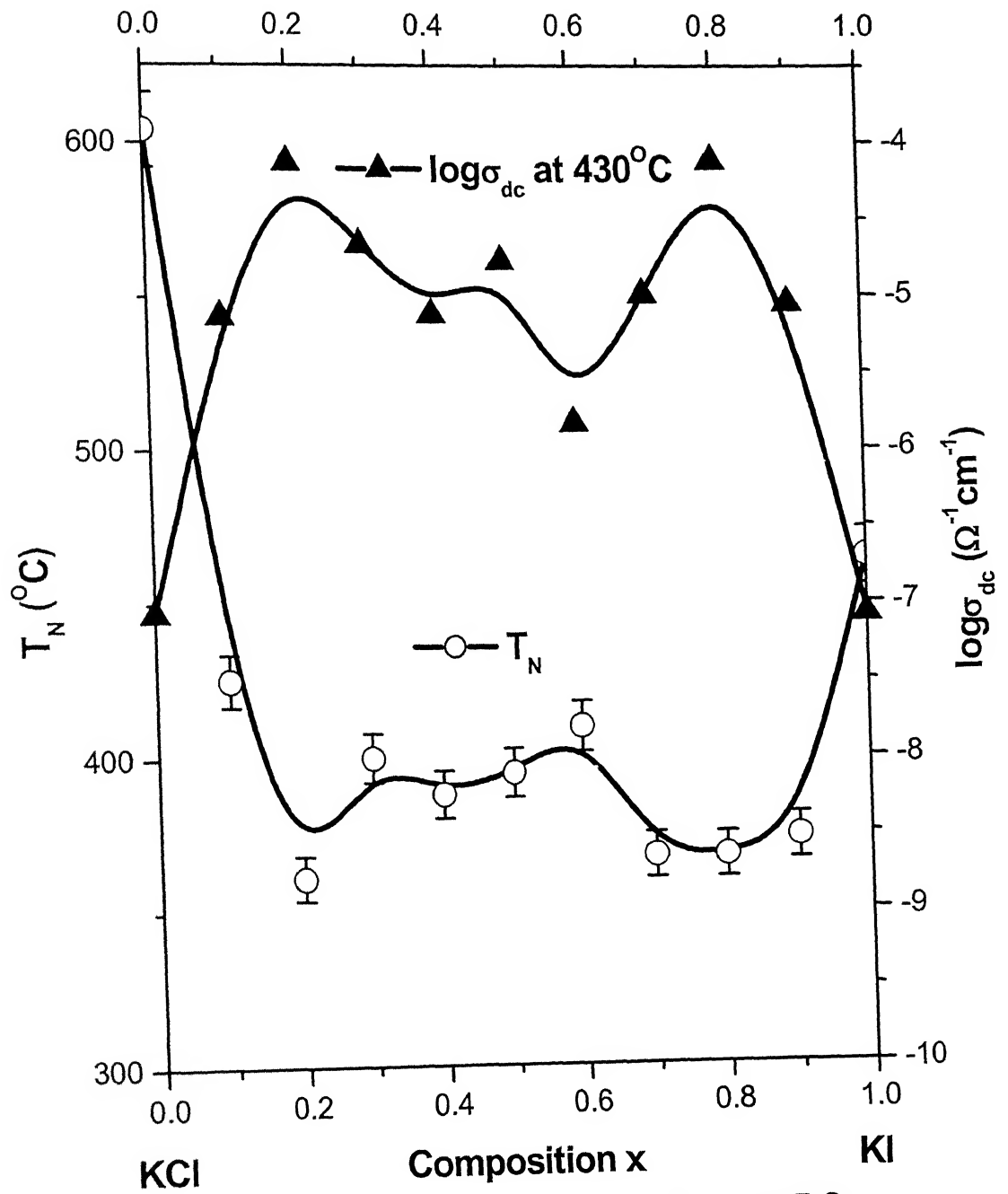


Fig. 4.11: Variation of knee temperature T_N and DC conductivity with composition plotted on the same graph.

(i.e. h_m and E_a) decrease along with the knee temperature T_N . As expected the h_m vs. x , E_a vs. x and T_N vs. x plots exhibit two minima at around the same compositions KCl + xKI ($x \approx 0.20$ in the two phase and $x \approx 0.80$ in the solid solution region) at which the $\log \sigma_{dc}$ vs. x plot exhibits maxima. These results are qualitatively in agreement with the Lattice Loosening model^[15].

4.5 Discussion

All the above experimentally observed features can be explained using Lattice Loosening (LL) model^[15] in the solid solution region and the percolation^[47] model in the two-phase region.

Lattice Loosening model predicts an increase in the conductivity in the solid solution region for a homovalently-doped salt due to strains produced in the lattice because of mismatch in the sizes of the host and the dopant ions. It states that the increase in conductivity varies exponentially with decrease in the melting point of the salt upon doping. According to the lattice loosening model, the relative conductivity varies exponentially with inverse absolute temperature [Eq. (2.50)].

Figures 4.12 to 4.14 show the experimental and calculated [using Eq. (2.50)] relative conductivities (σ_x/σ_0) vs. composition at three different temperatures (355, 400 and 430°C) for KCl-KI system.

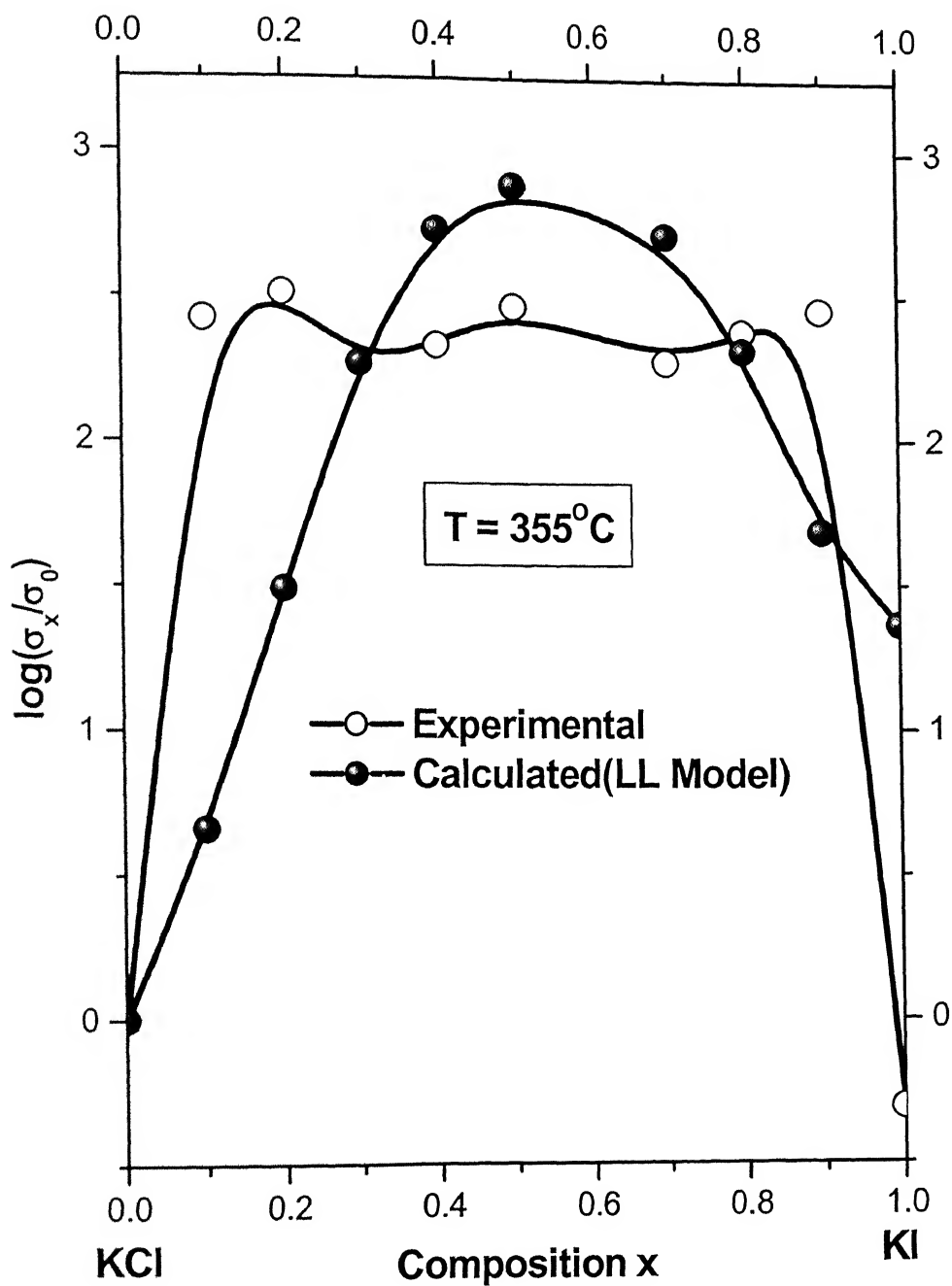


Fig 4.12: Comparison of Lattice Loosening model with the data obtained from experiment.

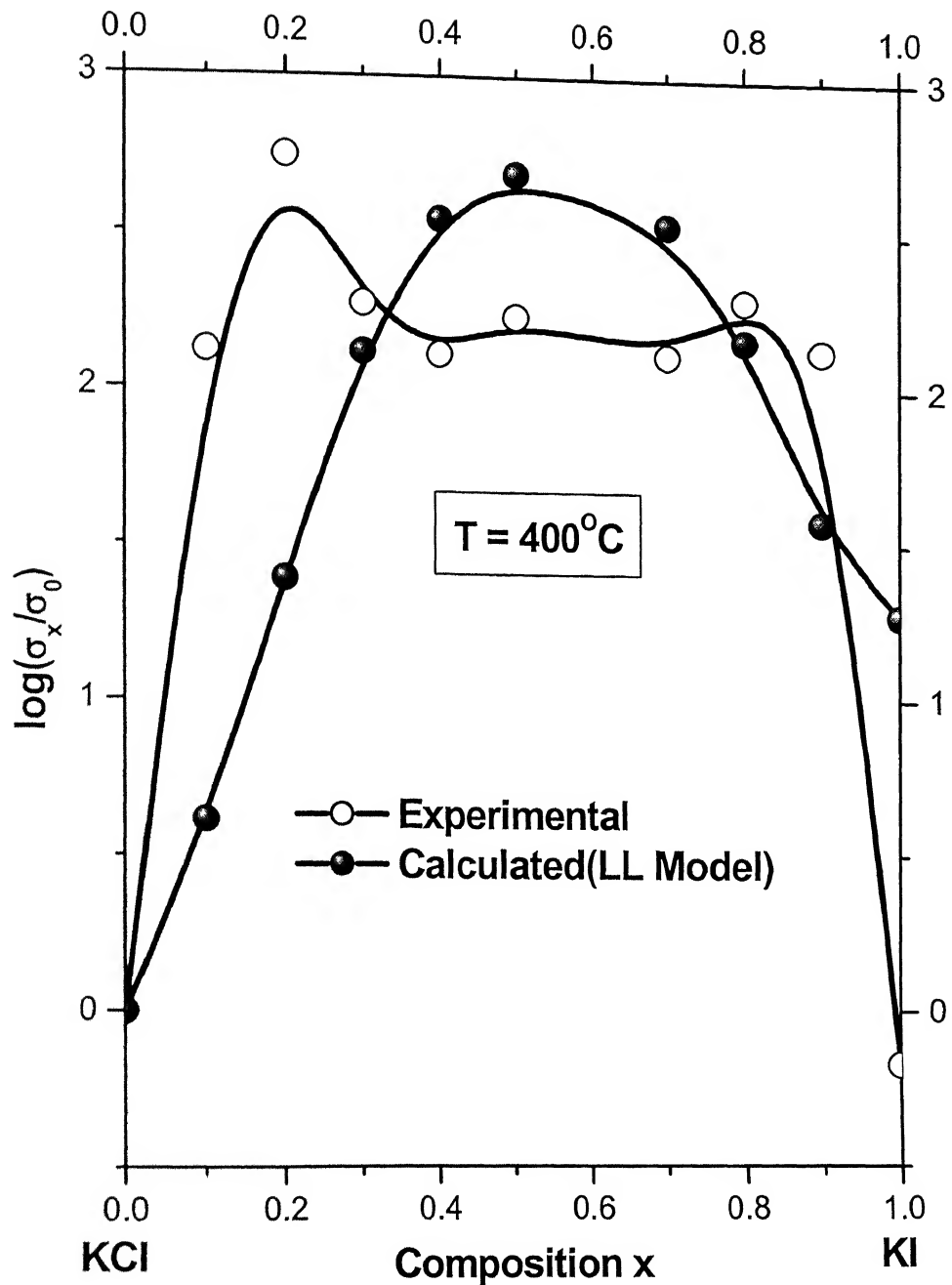


Fig 4.13: Comparison of Lattice Loosening model with the data obtained from experiment.

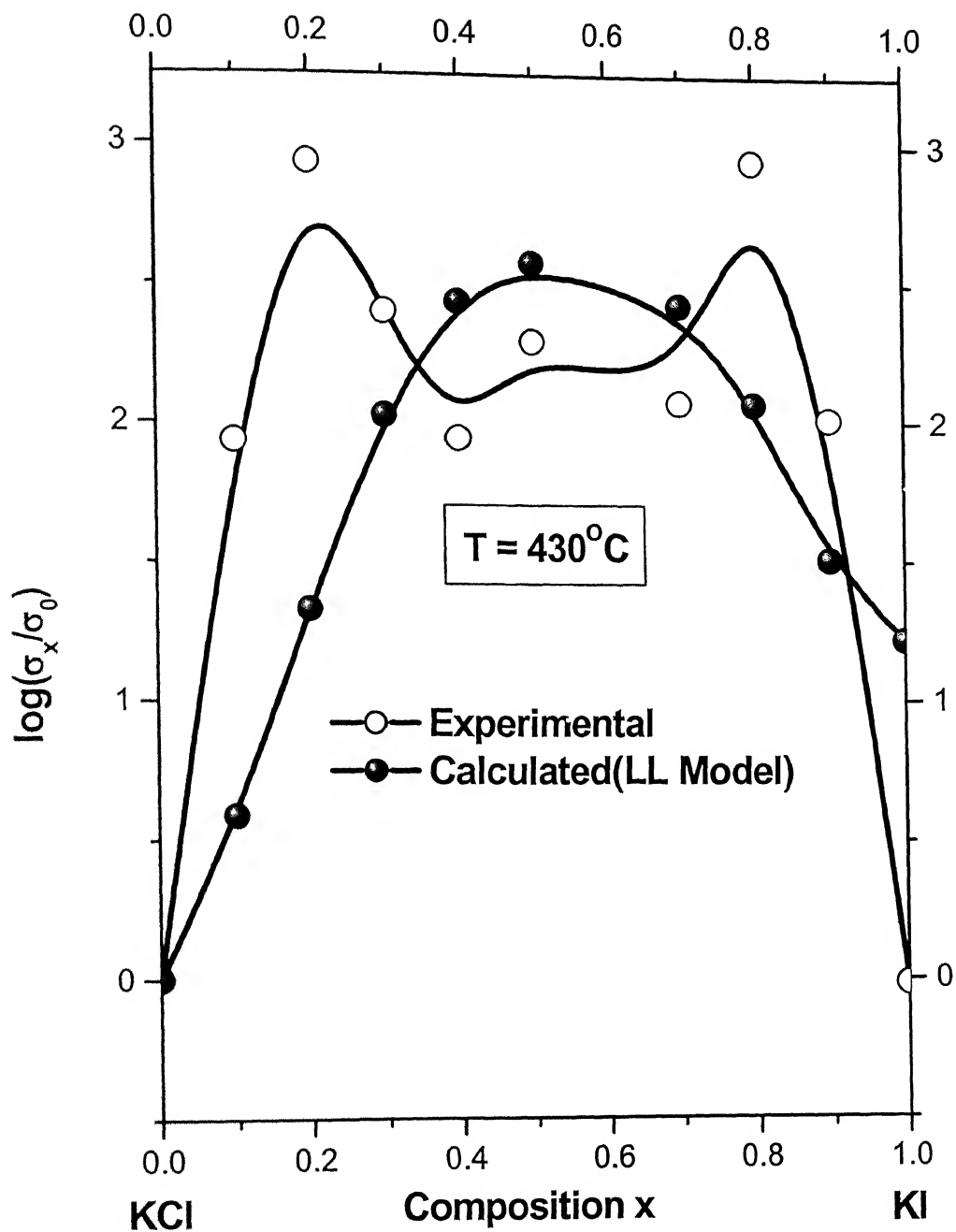


Fig 4.14: Comparison of Lattice Loosening model with the data obtained from experiment.

The conductivity studies which extend down to 300°C in a normal Arrhenius manner [Figs. 4.5(a-j)] suggest that the KCl-KI system may form a complete solid solution, at least above 300°C . But this fact is in contradiction with the available phase diagram^[40] [Fig. 4.2] where the two phase – solid solution boundary has been shown using dotted demixing curve. The phase diagram is too old (1912) and this has to be re-investigated using DTA technique to confirm the phase diagram. From the available phase diagram it can be seen that for compositions $0.1 < x < 0.7$ the two phase mixture always exists below 500°C . The conductivity measurements in the present case have been carried out up to $550\text{--}580^{\circ}\text{C}$ i.e., all our measurements are in the two-phase region for compositions KCl + xKI ($0.1 \leq x \leq 0.7$). Beyond 70 m/o KI all compositions are in solid solution region. The measurements could not be taken beyond $550\text{--}580^{\circ}\text{C}$ because of several experimental difficulties like poor graphite contact etc.

If we assume that above 300°C there is complete solid solubility over the entire composition range, then the LL model predicts results which are in reasonably good agreement with the experimental observations near the compositions where the conductivity passes through maxima. Table 4.8 shows close agreement between the calculated value of the relative conductivity using the LL model [Eq. (2.50)] and the data obtained from experiment at three different temperatures [Fig. 4.8] near to maximum conductivity compositions.

From the nature of Eq. (2.50) it is quite evident that the maximum enhancement in conductivity would occur where the solidus curve in the phase diagram passes through minimum. From the available phase diagram

[Fig. 4.2] it can be seen that the solidus curve has maximum at $x = 0.5$ KI composition. Therefore the conductivity isotherm should have maximum value at that composition according to the LL model. But in the present case the LL model is in close agreement at compositions close to the end members i.e., for the range of compositions $x \leq 0.3$ KI and $x \geq 0.8$ KI which can be easily inferred from Figs. 4.12-4.14 by observing the nature of the curve. The conductivity isotherms [Fig. 4.7] and the relative conductivity plots [Figs. 4.12-4.14] show two maxima near the compositions stated above. Further in the range $0.30 \leq x \leq 0.80$, the conductivity virtually

Table 4.8 Agreement of LL model with the experimental values obtained for KCl-KI system.

Composition x (KCl + xKI)	Experimental σ_x/σ_0 at $T(^{\circ}\text{C})$			Calculated σ_x/σ_0 from LL model at $T(^{\circ}\text{C})$		
	355	400	430	355	400	430
0.3	184	187	251	185	131	106
0.8	240	195	883	206	144	116

remains constant except at higher temperatures as in the case of Fig. 4.14, the curve slowly goes upward at $x = 0.5$ KI and then falls back again to pass through a maximum at $x = 0.8$ KI. The inconsistency between the conductivity isotherm and the phase diagram or the LL model in the composition range $x = 0.3 - 0.8$ KI, may be due to the poor correlation between H_s and T_m and between h and T_m [Eqs. (2.36) & (2.43)]. Moreover in the above range we have assumed the composition to be in the solid solution region which is in contradiction with the available phase diagram

[Fig. 4.2]. Various approximations have been used to derive Equation (2.50) which can be attributed to the anomaly in the composition range $0.3 < x < 0.8$.

Our estimated solidus curve on the basis of the data extracted from the conductivity measurements is compared with the one from phase diagram in Fig 4.15. The conductivity isotherm at 430°C has also been plotted on the same graph to show the correlation. The estimated solidus curve has been plotted by assuming that melting of the sample begins when the conductivity value reaches a magnitude of $10^{-3} \Omega^{-1}\text{cm}^{-1}$. So the estimated melting temperatures have been obtained by simply reading off the temperature corresponding to $\log\sigma_{dc} = -3$ from each Arrhenius plot. Though this is a very crude approximation and the estimated solidus curve does not follow the solidus curve of the phase diagram at each composition, the conductivity behavior (and the activation energy and the knee temperature) can be well explained by this estimated solidus curve. It is quite evident from Fig. 4.15 that the two maxima in the $\log\sigma_{dc}$ vs. x plot correspond to same compositions where the estimated solidus curve shows minima. This phenomenon is qualitatively at par with the LL model.

The temperature T_{σ} at which the system attains a certain fixed value of conductivity (σ) is shown as a function of composition in Fig. 4.16. The T_{σ_1} and T_{σ_2} curves corresponding to $\sigma_1 = 10^{-5} \Omega^{-1}\text{cm}^{-1}$ and $\sigma_2 = 3 \times 10^{-5} \Omega^{-1}\text{cm}^{-1}$ respectively are constructed from the data shown in Fig. 4.5[a-j]. The solidus curve T_{mx} of the phase diagram and the estimated solidus curve T_m from

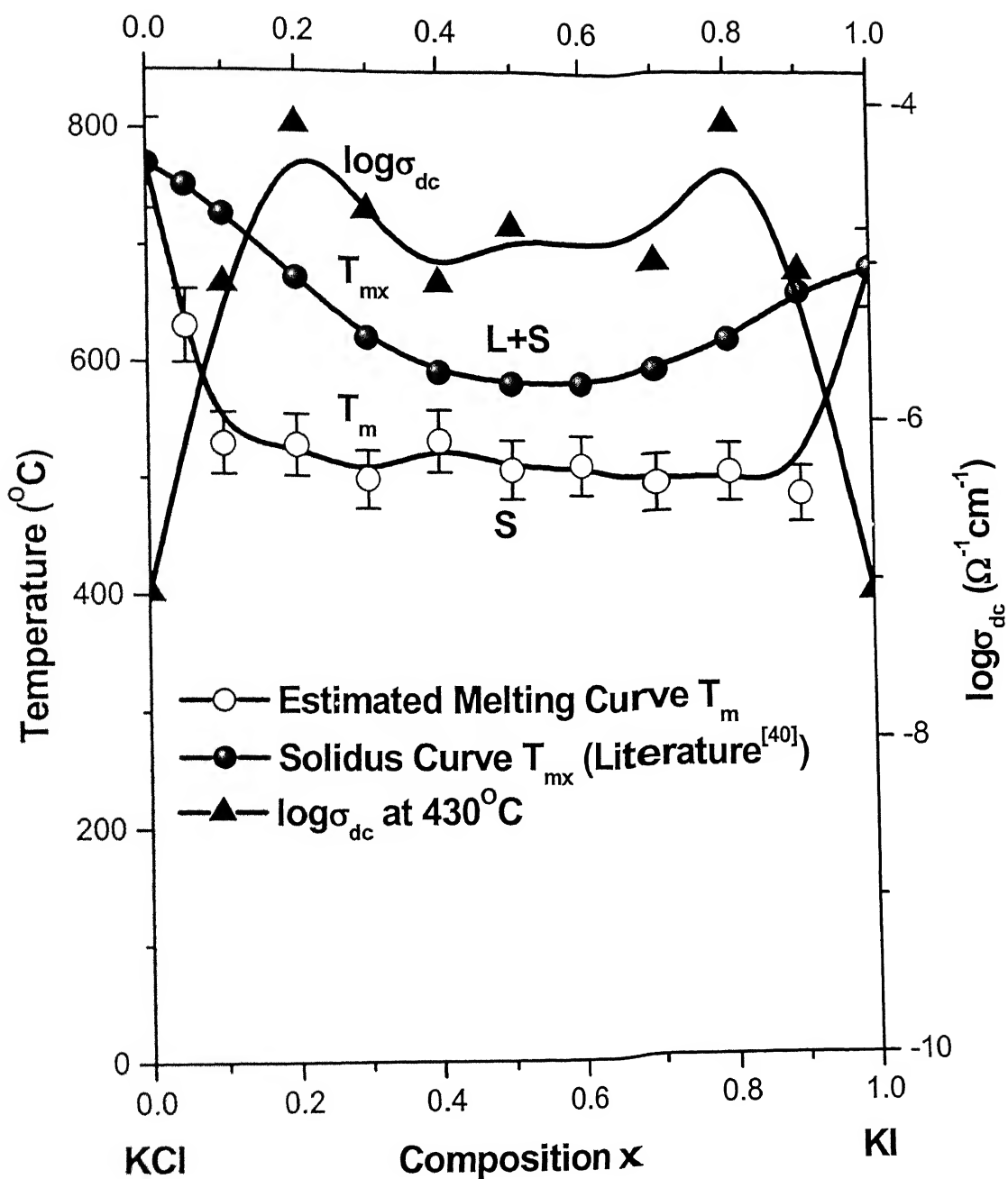


Fig 4.15: Estimated melting temperature obtained from conductivity data. The solidus curve from available phase diagram has also been shown with the conductivity isotherm at 430°C.

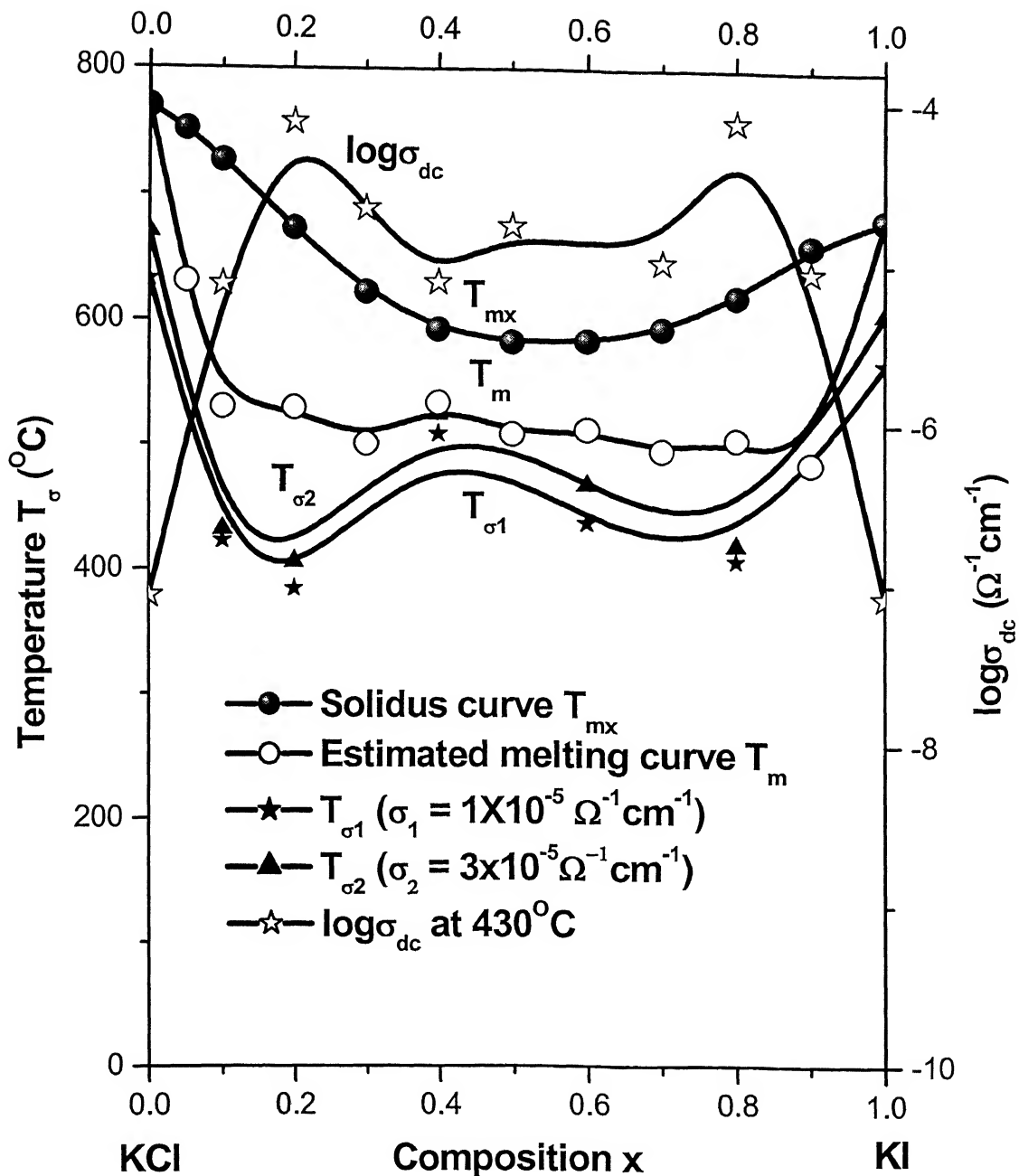


Fig 4.16: Isoconductivity plots for KCl - KI system.
 The solidus curve T_{mx} obtained from literature^[40] and the estimated melting curve from conductivity data can also be seen with one conductivity isotherm.

conductivity data along with the conductivity isotherm at 430°C have been shown on the same graph for better correlation. The resemblance between the T_{σ} vs. x , T_{mx} vs. x (i.e., occurrence of a minimum between two maxima) and T_m vs. x along with the results shown in Figs. 4.9, 4.10 and 4.11 provide support to the LL model. The discrepancy becomes less if the estimated solidus curve is considered for correlation (Fig. 4.16).

According to the $\text{CB}\Omega$ model (see Sec. 2.3.2.2) the composition x_m corresponding to the maximum conductivity is given by [Eq. (2.52)]

$$x_m = \frac{\left(\frac{k_d}{k_o}\right) - 2}{\lambda \left(\frac{k_d}{k_o}\right)}$$

Substituting $\lambda = 0.4163$ and $K_d/K_o = 2.282$ for KCl-KI system [these values were calculated by Smith and Cain^[53] and Roberts and Smith^[54]] in the above equation we get,

$$x_m = 0.29$$

Thus, according to the $\text{CB}\Omega$ model, KCl containing $x = 0.29$ KI should exhibit the maximum conductivity which is not too far from the value $x \approx 0.20$ KI inferred from the experiments [Fig. 4.7].

Alternately, if we consider the KCl as the dopant in KI for which $K_d/K_o = 2.305$, we get $x_m = 0.32$. Therefore KI containing ≈ 0.32 KCl should have the maximum [or KCl containing 0.68 KI] conductivity which is in good agreement with the observed value ($x \approx 0.80$ KI).

The variation of activation energy as a function of composition and the conductivity isotherms in the composition range $0.1 < x < 0.7$ i.e., in the two phase region can be explained using the percolation model^[47]. The percolation model states that in a two-phase system, there exists a minimum concentration of the dopant, the percolation threshold, until which there is no enhancement in the conductivity of the system. The percolation threshold corresponds to the minimum concentration at which there is a continuum of charged double layer formed. The percolation threshold should obviously depend on the grain size, which depends on the heating/cooling rate. From the conductivity isotherms (Fig. 4.7) the percolation threshold for KI dispersed in KCl is achieved for a composition between 20 and 25 m/o KI. The heating rate employed was $0.5^{\circ}\text{C}/\text{min}$ for all the samples. Further studies with samples prepared under controlled cooling rate will be required to determine percolation threshold precisely. The minimum in the activation energy vs. composition plots (Figs. 4.9 & 4.10) and the maximum in the conductivity isotherms in these plots that are observed at $x \approx 0.20$ KI in the two phase region can be attributed to the formation of a continuous charged double layer beyond the percolation threshold.

The enhancement in the conductivity in the two-phase region is due to the formation of a double layer, rich in defects, at the grain boundaries where two dissimilar phases come into contact with each other^[48]. The conductivity of the double layer at the interfaces is supposedly greater than that of either of the phases present in the system. At very low concentrations of the second phase particles, the conductivity of the system does not change in spite of the formation of the double layer, because of the lack of continuous channels for migration of the defects. As mentioned earlier, the critical concentration

required for the formation of a continuous double layer is the percolation threshold. As the concentration of second phase increases beyond the threshold, the second phase particles might not contribute to the formation of additional interfacial region, but might increase the thickness of the second phase around the double layer. Since the second phase has a lower defect concentration than the double layer, the conductivity of the system decreases. The local minimum near to $x \approx 0.40$ KI in the conductivity isotherm may be due to the increase in the thickness of β phase (KCl solid solution with KI) around the double layer.

Table 4.9 shows the mismatch factor δ and the maximum enhancement in conductivity at 400°C for various homovalent systems. A comparative idea can be had from this Table and it can be ascertained that the results obtained for the present case are quite comparable and reasonable within the experimental error.

4.6 Summary & Conclusion

Fourteen samples of $\text{KCl}_{1-x}\text{I}_x$ ($0 \leq x \leq 1.0$) have been prepared by normal melting the constituent powders and then allowing it to cool inside the furnace. Some samples have been quenched for investigating any change in the ionic conductivity. Different techniques were used to characterize the samples which include XRD, BET, FT-IR and complex impedance analysis. The XRD patterns of KCl-KI system showed that at least 30 m/o KCl goes into solid solution with KI, which is supported by the available phase diagram. The phase diagram also suggests that KCl-KI system does not form

complete solid solution below certain temperatures for all the compositions. Instead there is always a presence of complete or partial solid solution. Therefore both types of compositions are always present in the temperature range of our measurement of conductivity (i.e., $300^{\circ}\text{C} - 525^{\circ}\text{C}$) one being the two phase region up to $x = 0.7$ KI and the other a complete solid solution region beyond that.

Table 4.9 Conductivity enhancement and mismatch factor for similar systems employing homovalent substitution.

System	σ_x/σ_0 at x_m at 400°C	x_m	$\delta = (1 - r_d/r_h)$
KBr-KI ^[9]	63	0.50	0.12
KBr-KCl ^[46] (single crystal)	1.5	0.32	0.08
NaCl-NaBr ^[49]	15	0.60	0.08
NaBr-NaI ^[49]	35	0.70	0.12
LiBr-LiI ^[11]	34	0.40	0.12
KCl-KI (present work)	430	0.20	0.21
NaBr-LiBr ^[49]	8000	0.70	0.30
KBr-NaBr ^[49]	34	0.50	0.27
KBr-NaI ^[49]	853	0.70	-

The crystallite sizes were analyzed from the XRD data using PeakFit V. 4.0 for nearly all the compositions, which vary from 37 nm to 70 nm.

The FT-IR analysis confirmed presence of OH group in all the samples as expected because both the constituent powders are very hygroscopic. The impurities present in KI-rich samples can also be ascertained from FT-IR though in the available range of wave numbers ($400 - 4000\text{ cm}^{-1}$) both the halides are not IR sensitive.

BET measurements offered the magnitude of specific surface area. The specific surface area seems to increase with m/o KI which suggests smaller grains for compositions with higher concentration of KI and thus yielding higher conductivity which is evident for the case of $KCl + 0.8\text{ KI}$. The overall low values of specific surface area indicate that the surface contact between electrode and electrolyte may be poor which might affect the accuracy of measurement of conductivity.

DC conductivity at a particular temperature was measured using CIA. All the plots of $\log \sigma_{dc}$ vs. $1/T$ showed normal Arrhenius manner in which two distinct slopes are present separated by a knee point.

In the present system, a maximum enhancement of σ by a factor of 430 and 169 (i.e., more than two orders of magnitude) with respect to pure KCl is observed at 400°C for $KCl + 0.2\text{ KI}$ in the two-phase region and for $KCl + 0.8\text{ KI}$ in the solid solution region respectively. The conductivity enhancement in the two-phase region can be explained using percolation model. Lattice Loosening model explains the conductivity enhancement in the solid solution region very well. The close agreement between the observed and the calculated σ_x/σ_0 (Figs. 4.12-4.14) and the close

resemblance between the T_σ vs. x (Fig. 4.16), melting temperature T_m vs. x (Fig. 4.15), $\log \sigma_{dc}$ vs. x along with T_N , h_m , E_a vs. x (Figs. 4.9, 4.10 & 4.11) provide strong support to the LL model. The $CB\Omega$ model is found to predict the composition corresponding to the maximum conductivity quite accurately.

More precise measurements in the solid solution region, $0.1 \geq x \geq 0.7$, preferably on mixed single crystals, seem highly desirable.

References

1. C. Tubandt and E. Lorentz, *Z. Phys. Chem.* **87** (1914) 513
2. S. Chandra (1981), *Superionic Solids*, North Holland Publishing Company, Amsterdam.
3. A. Kvist, *Z. Naturf.* **22a** (1967) 208
4. K. Shahi and J. B. Wagner Jr., *J. Electrochem. Soc.* **128** (1981) 6
5. K. Shahi and J. B. Wagner Jr., *Phys. Rev. B* **12** (1981) 6417
6. S. Chaklanobis, R. K. Syal and K. Shahi, *Solid State Ionics* **44** (1990) 107
7. G. Prakash and K. Shahi, *Solid State Ionics* **23** 151
8. C. C. Liang, *J. Electrochem. Soc.* **120** (1973) 1289
9. K. Shahi and J. B. Wagner Jr., *J. Phys. Chem. Solids* **44** (1983) 89
10. J. B. Holt, H. G. Sockel and H. Schmalzried, *J. Am. Ceram. Soc.* **52** (1969) 375
11. S. Gupta, S. Patnaick, S. Chaklanobis and K. Shahi, *Solid State Ionics* **31** (1988) 5
12. T. Bhima Sankaram and K. G. Bansigiri, *Crystal Lattice defects* **7** (1978) 209
13. A. Schiraldi, E. Pezzati and G. Chiodelli, *Z. Physik. Chem. neu folge* **110** 1 as cited by P. Manoravi in his PhD thesis (1991, IIT Kanpur)
14. K. Shahi and J. B. Wagner Jr., *J. Phys. Chem. Solids* **43** (1982) 713
15. K. Shahi and J. B. Wagner Jr., *J. Solid State Chem.* **42** (1982) 107
16. S. Ihara, Y. Warita and K. Suzuki, *Phys. Stat. Solidi A* **86** (1984) 729
17. R. Mercier, M. Tachz, J. P. Malguani and G. Robert, *Solid State Ionics* **15** (1985) 109
18. V. N. Erofeev and E. Hartmann, *Solid State Ionics* **28** (1988) 241

- 19.P. Manoravi and K. Shahi, *J. Phys. Chem. Solids* **52** (1991) 527
- 20.P. Varotsos, W. Ludwig and K. Alexopoulos, *Phys. Rev. B* **18** (1978) 2683
- 21.P. Varotsos, *J. Phys. Chem. Solids* **42** (1981) 405
- 22.P. A. Varotsos and K. D. Alexopoulos (1986), “*Thermodynamics of point defects and their relations with bulk properties*”, North – Holland, Amsterdam.
- 23.M. Lazaridou and C. Varotsos, *J. Phys. Chem. Solids* **46** (1985) 643
- 24.A. B. Lidiard (1957), In “*Handbuch der physik*”, (Ed. Flugge. S), Vol. 20, p. 246, Springer-verlag, Berlin.
- 25.H. R. Glyde, *Rev. Mod. Phys.* **39** (1967) 373
- 26.R. J. Friauf (1972), In “*Physics of Electrolytes*”, (Ed. Hladik J.), Vol 1 & 2, Academic Press, New York and London.
- 27.E. Koch and C. Wagner, *Z. Phys. Chem. Abt. B* **38** (1937) 295
- 28.H. Kelting and H. Witt, *Z. Physik* **126** (1949) 697
- 29.J. Teltow, *Ann. Phys. Lpz.* **5** (1949) 63
- 30.S. Chandra and J. Rolfe, *Can. J. Phys.* **48** (1970) 397
- 31.S. Chandra and J. Rolfe, *Can. J. Phys.* **48** (1970) 412
- 32.Johannesen and M. McKelvy, *J. Phys. Chem. Solids* **47** (1986) 265
- 33.Johannesen, *Proc. of the 6th Int. Conf. on Solid State Ionics*, Garmische-Partenkirchen, FRG, Sept. 6-11 (1987), p. 1310
- 34.L. W. Barr and A. B. Lidiard, In “*Physical Chemistry - An Advanced Treatise*”, (Ed. W. Jost), Academic Press, New York, Vol. 10 (1970), p. 151
- 35.W. Bollmann, N. F. Uvarov and E. F. Hairetdinov, *Cryst. Res. Technology* **24** (1989) 421
- 36.W. E. Wallace and R. A. Flinn, *Nature* **172** (1953) 681

- 37.J. B. Holt, H. G. Sockel and H. Schmalzried, *J. Am. Ceram. Soc.* **52** (1969) 375
- 38.L. W. Barr and D. K. Dawson, *Proc. Britt. Ceramic. Soc.* **19** (1971) 151 as cited by P. Manoravi in his PhD thesis.
- 39.F. Beniere and V. Haribabu, *Cryst. Latt. Defects and Amorph. Mat.* **15** (1987) 263
- 40.Phase Diagrams for Ceramists, M. K. Reser (Ed.), The American Ceramic Society, Columbus, Ohio (1964)
- 41.C. S. Smith and R. W. Roberts, In “Generalized Born Model”, Atomic Energy Commission Tech, Rep. No 1(Contract No. AT 40-I-3802) (1968)
- 42.J. R. MacDonald (ed.), “Impedance Spectroscopy”, John Wiley & Sons, Vol. 1, 2 (1987)
- 43.E. S. Barr (ed.), “Infrared Physics”, Vol 1, 1 (1961)
- 44.W. I. Archer and R. D. Armstrong, *Electrochemistry* **7** (1980) 157
- 45.A. Hooper, *J. Phys. D* **10** (1977) 1487
- 46.Johannesen, *Solid State Ionics* **28-30** (1988) 1310
- 47.A. Bunde, W. Dieterich and H. E. Roman, *Solid State Ionics* **18/19** (1986) 147
- 48.T. Jow and J. B. Wagner Jr., *J. Electrochem. Soc.* **126** (1979) 1963
- 49.P. Manoravi, PhD Thesis (1991), IIT Kanpur, India
- 50.J. Frenkel, *Z. Physik.* **35** (1926) 652
- 51.W. Schottky, *Z. Phys. Chem. Abst.* **B29** (1935) 335
- 52.Y. Haven, In “Report of the Conference on Defects in Crystalline Solids” held at Bristol in July 1954, p 261, London (1957)
- 53.C. S. Smith and L. S. Cain, *J. Phys. Chem. Solids.* **36** (1975) 205

- 54.R. W. Roberts and C. S. Smith, *J. Phys. Chem. Solids.* **31** (1970) 619
- 55.J. E. Bauerle, *J. Phys. Chem. Solids.* **30** (1969) 2657